

NONLINEAR EVOLUTION OF HYDRODYNAMICAL SHEAR FLOWS IN TWO DIMENSIONS

YORAM LITHWICK¹
Draft version October 22, 2018

ABSTRACT

We examine how perturbed shear flows evolve in two-dimensional, incompressible, inviscid hydrodynamical fluids, with the ultimate goal of understanding the dynamics of accretion disks, as well as other astrophysical shear flows. To linear order, vorticity waves are swung around by the background shear, and their velocities are amplified transiently before decaying. It has been speculated that sufficiently amplified modes might couple nonlinearly, leading to turbulence. Here we show how nonlinear coupling occurs in two dimensions. This coupling is remarkably simple because it only lasts for a short time interval, when one of the coupled modes is in mid-swing, i.e., when its phasefronts are aligned with the radial direction. We focus on the interaction between an axisymmetric mode and a swinging mode. We find that all axisymmetric modes, regardless of how small in amplitude, are unstable when they interact with swinging modes that have sufficiently large azimuthal wavelength. Quantitatively, the criterion for instability is that $|k_{y,sw}/k_{x,axi}| \lesssim |\omega/q|$, i.e., that the ratio of wavenumbers (swinging azimuthal wavenumber to axisymmetric radial wavenumber) is less than the ratio of the perturbed vorticity to the background vorticity. If this is the case, then when the swinging mode is in mid-swing it couples with the axisymmetric mode to produce a new leading swinging mode that has larger vorticity than itself; this new mode in turn produces an even larger leading mode, etc. We explain how this shear (or Kelvin-Helmholtz) instability operates in real-space as well. The instability occurs whenever the momentum transported by an energy conserving perturbation has the sign required for it to diminish the background shear; only when this occurs can energy be extracted from the mean flow and hence added to the perturbation. For an accretion disk, this means that the instability transports angular momentum outwards while it operates. We verify all our conclusions in detail with full hydrodynamical simulations, done with a pseudospectral method in a shearing box. Simulations of the instability form vortices whose boundaries become highly convoluted. Whether this nonlinear instability plays a role in accretion disks is an interesting possibility.

Subject headings: accretion, accretion disks — instabilities — solar system: formation — turbulence

1. INTRODUCTION

Matter accretes onto a wide variety of objects, such as young stars, black holes, and white dwarfs, through accretion disks. For matter in an accretion disk to fall inwards, angular momentum must be transported outwards. In many accretion disks, it is turbulence and the resulting turbulent viscosity that is responsible for angular momentum transport. Therefore, if one wishes to understand accretion disks, one must first address how disks become turbulent, and how much turbulence they sustain. In highly ionized disks, magnetic fields can trigger turbulence via the magnetorotational instability (Balbus & Hawley 1998). However in neutral (hydrodynamical) disks, the situation is unclear. It remains an open question whether neutral Keplerian disks are turbulent, or whether they can remain laminar despite enormous Reynolds numbers. Until it is answered, the accretion of nearly neutral disks, such as those around young stars (e.g., Sano et al. 2000) or dwarf novae (e.g., Gammie & Menou 1998), will remain mysteries. Simulations (Hawley et al. 1999; Shen et al. 2006) and experiments (Ji et al. 2006) both point to the answer that incompressible hydro disks are laminar—or at least that any turbulence in them would not be strong enough to act as the agent of angular momentum transport (Lesur & Longaretti 2005). But the evidence is not conclusive because the Reynolds numbers in disks are much

larger than those accessible to computers or experiments.

Even if one takes the view that numerical and experimental evidence rules out self-sustaining incompressible turbulence in Keplerian disks, it remains important to understand how such shear flows work. In our view, this is an essential first step before more complicated effects—such as baroclinic effects, convection, stirring by planets, stirring by dust, or stirring by a magnetically active layer above the midplane—can be understood. It could be that one of these effects is responsible for turbulence in disks. In the present paper, we describe in detail the dynamics of perturbations in incompressible shear flows in two dimensions (in the plane of the disk). Even though 2D flows do not lead to turbulence, they exhibit a remarkably rich dynamics. Of course, incompressible 2D shear flows have been the subject of an enormous amount of research (e.g., Drazin & Reid 2004). But our methods are different: we calculate the nonlinear coupling between linear waves. One of the benefits of this approach is that it is straightforward to generalize it to three dimensions, as well as to include effects such as compressibility and magnetohydrodynamics.

Recently, the evolution of linear waves has been the focus of much attention in the astrophysical literature. Since the velocity field of a linear swinging wave can be amplified by very large factors during its swing, it has been proposed that sufficiently amplified modes

¹ CITA. Toronto, Ontario, Canada; yoram@cita.utoronto.ca

might couple nonlinearly, leading ultimately to turbulence (e.g., Ioannou & Kakouris 2001; Chagelishvili et al. 2003; Umurhan & Regev 2004; Yecko 2004; Afshordi et al. 2005). However, how this coupling might occur has not been discussed (though see Mukhopadhyay 2006), nor has the amplitude needed to trigger nonlinear effects been quantified. The present paper begins to rectify these shortcomings. Balbus & Hawley (2006) show that linear swinging waves are exact solutions of the nonlinear equations of motion. They contend that this argues against transient amplification as a route to turbulence in unmagnetized disks. However, we show in the present paper that nonlinear coupling between two different waves can lead to interesting dynamics even when the individual waves are exact nonlinear solutions.

Numerical simulations of 2D shear flows starting from random initial conditions settle into a distinctive banded structure (Umurhan & Regev 2004; Johnson & Gammie 2005; Shen et al. 2006). Roughly speaking, bands where $\omega > 0$ are interspersed with bands where $\omega < 0$ (ω is the perturbed vorticity, eq. [7]). Bands where ω has the same sign as the background vorticity contain a single vortex; in bands with the opposite sign, ω is smooth and there are no vortices. One of the goals of this paper is to explain why this is a natural outcome of random initial conditions.

1.1. Organization

We introduce the equations of motion in §2. In §§3-5, the heart of this paper, we describe and simulate the nonlinear coupling between modes, focusing on the shear instability that results from the coupling between swinging waves and axisymmetric ones. In §6, which can be read independently of §§3-5, we describe the instability in real space. We give both a dynamical explanation and one based on momentum and energy arguments. We also simulate the fully nonlinear outcome of the instability. We conclude in §7. In the Appendix, we describe the pseudospectral code that we use to run simulations in §§3-5.

2. EQUATIONS OF MOTION

An unperturbed Keplerian disk has angular velocity profile $\Omega(r) \propto r^{-3/2}$. We write the fluid equations in a reference frame rotating at constant angular speed $\Omega_0 \equiv \Omega(r_0)$, where r_0 is a fiducial radius, and replace the radial and azimuthal coordinates r, θ with Cartesian coordinates, $x \equiv r - r_0$, $y \equiv r_0\theta$. On lengthscales much smaller than r_0 , the “shearing box” equations of motion for an incompressible fluid are

$$\begin{aligned} \partial_t \mathbf{v} + \mathbf{v} \cdot \nabla \mathbf{v} &= -2\Omega_0 \hat{\mathbf{z}} \times \mathbf{v} + 2q\Omega_0 x \hat{\mathbf{x}} - \nabla(P/\rho) \quad , \quad (1) \\ \nabla \cdot \mathbf{v} &= 0 \quad , \quad (2) \end{aligned}$$

where \mathbf{v} is the velocity field in the rotating frame and

$$q \equiv - \left. \frac{d\Omega}{d \ln r} \right|_{r_0} = \frac{3}{2} \Omega_0 \quad . \quad (3)$$

We use standard Cartesian vectorial notation, e.g., $\mathbf{v} = v_x \hat{\mathbf{x}} + v_y \hat{\mathbf{y}} + v_z \hat{\mathbf{z}}$, etc. The first term on the right-hand side of equation (1) is the Coriolis force, and the second is what remains after adding the centrifugal and gravitational forces.

² In the non-rotating frame, the unperturbed disk has total velocity field $\mathbf{v}_{\text{tot}} = r\Omega_0 \hat{\boldsymbol{\theta}}$, and the corresponding vorticity is $\hat{\mathbf{z}} \cdot \nabla \times \mathbf{v}_{\text{tot}} = d\Omega/d \ln r + 2\Omega = -q + 2\Omega_0$ at r_0 . This differs from equation (10) (by $2\Omega_0$) because of the change in reference frame.

³ This restriction precludes us from seeing the shear (or Kelvin-Helmholtz) instability discovered by Shen et al. (2006), which requires $|\omega| \gtrsim q$.

Decomposing the fluid velocity into

$$\mathbf{v} = -qx\hat{\mathbf{y}} + \mathbf{u} \quad , \quad (4)$$

where the first term is the shear flow of the unperturbed disk, yields

$$\begin{aligned} (\partial_t - qx\partial_y) \mathbf{u} + \mathbf{u} \cdot \nabla \mathbf{u} &= 2\Omega_0 u_y \hat{\mathbf{x}} - (2\Omega_0 - q) u_x \hat{\mathbf{y}} - \nabla(P/\rho) \\ \nabla \cdot \mathbf{u} &= 0 \end{aligned} \quad (6)$$

We shall solve these equations in two dimensions, in the $x - y$ plane. It is simpler, though, to work with the curl of equation (5), which may be expressed in terms of vorticity of \mathbf{u} ,

$$\omega \equiv \hat{\mathbf{z}} \cdot (\nabla \times \mathbf{u}) \equiv \partial_x u_y - \partial_y u_x \quad , \quad (7)$$

as follows:

$$(\partial_t - qx\partial_y)\omega + \mathbf{u} \cdot \nabla \omega = 0 \quad , \quad (8)$$

with \mathbf{u} given by the inverse of equation (7):

$$\mathbf{u} = \hat{\mathbf{z}} \times \nabla \nabla^{-2} \omega \quad . \quad (9)$$

Equations (8)-(9) form a complete set. This paper is devoted to solving them.

Equation (8) shows that ω is advected by the total velocity field $-qx\hat{\mathbf{y}} + \mathbf{u}$. Vorticity is locally conserved in two dimensions (in the absence of dissipation); ω is neither created nor destroyed, but is simply shuffled around by the velocity field that it induces via equation (9). Therefore in 2D investigations one is forced to specify an initial vorticity field, and then to see how it is shuffled itself around. In three dimensions, vorticity might be created by turbulence, or by stirring by planets, or by convection. But the creation of vorticity is beyond the scope of this paper.

The vorticity of the unperturbed flow in the rotating frame² is

$$\hat{\mathbf{z}} \cdot \nabla \times (-qx\hat{\mathbf{y}}) = -q \quad ; \quad (10)$$

q sets a scale for the vorticity against which the strength of the perturbation ω may be measured. Throughout this paper, we restrict the perturbed vorticity to be less than the background vorticity³,

$$|\omega| \lesssim q \quad . \quad (11)$$

It is conceivable that hydrodynamic disks are so turbulent that they violate this inequality. But if they reach such a state via a nonlinear instability, then the instability would have had to act while the inequality held. Because of the above inequality, it is tempting to drop the nonlinear term $\mathbf{u} \cdot \nabla \omega$ from equation (8). However, we shall show that even when $|\omega| \ll q$ the nonlinear term is important provided that ω is sufficiently elongated in the streamwise direction. While we may indeed neglect nonlinear advection in the y -direction ($u_y \partial_y \omega$), the term $u_x \partial_x \omega$ advects fluid in a direction orthogonal to the background shear. The net displacement in x can be significant if u_x acts coherently over a large range in y .

2.1. Equivalence with Non-rotating Linear Shear Flows

Equations (8)-(9) also describe the dynamics of *non-rotating* incompressible 2D linear shear flows. To see this, one may discard the first two terms on the right-hand side of equation (1) and make the decomposition of equation (4), where the unperturbed shear rate q may now be set to any arbitrary constant. Equation (5) is then reproduced without the coriolis terms ($= -2\Omega_0 \hat{\mathbf{z}} \times \hat{\mathbf{u}}$). But the curl of this equation still yields equation (8), because in two dimensions the coriolis force is the gradient of a scalar, $-2\hat{\mathbf{z}} \times \mathbf{u} = \nabla \nabla^{-2} 2\omega$. Therefore the coriolis force can be absorbed into a redefinition of the pressure, and does not affect the dynamics. (The sum of centrifugal and gravitational forces $2q\Omega_0 \mathbf{x}$ also does not contribute to the dynamics of \mathbf{u} —it merely cancels the coriolis force due to the background shear $-2\Omega_0 \hat{\mathbf{z}} \times (-qx\hat{\mathbf{y}})$. But this is true in 3D as well. In fact, this balance sets the unperturbed velocity field.)

Rotating and non-rotating incompressible shear flows are equivalent only in two dimensions. To illustrate how this equivalence breaks down in three dimensions, we examine linear axisymmetric waves. In non-rotating shear flows (eq. [5] without the coriolis force), such “waves” have dispersion relation $\omega = 0$, and eigenfunction $\mathbf{u} \propto \hat{\mathbf{y}}$. They are static disturbances of the background flow that merely alter the shear flow’s velocity profile. Rotating shear flows have dispersion relation $\omega^2 = 2\Omega_0(2\Omega_0 - q)k_z^2/k^2$. Therefore two-dimensional modes (with $k_z = 0$) have $\omega = 0$ whether or not the flow is rotating. But axisymmetric modes in rotating flows with $k_z \neq 0$ have a non-zero frequency. When three dimensional motions are allowed, the coriolis force induces epicyclic-like oscillations.

3. NONLINEAR MODE COUPLING EQUATION

We solve equations (8)-(9) in a box of size $L_x \times L_y$ subject to boundary conditions that are periodic in y , and shifted periodic in x (eq. [A5]). Lagrangian coordinates (\mathbf{X}, T) shear with the background flow:

$$Y \equiv (y + qtx) \bmod L_y \quad (12)$$

$$(X, T) \equiv (x, t) \quad (13)$$

$$\Rightarrow \partial_T = \partial_t - qx\partial_y \quad (14)$$

The Fourier transform of ω with respect to Lagrangian coordinates is

$$\omega_{J_x, J_y} \equiv \int_0^{L_x} \int_0^{L_y} \frac{dX}{L_x} \frac{dY}{L_y} \omega(\mathbf{X}) e^{-i\mathbf{K} \cdot \mathbf{X}} \quad (15)$$

where

$$K_x \equiv \frac{2\pi J_x}{L_x}, \quad K_y \equiv \frac{2\pi J_y}{L_y} \quad (16)$$

for integer J_x, J_y , with inverse

$$\omega(\mathbf{X}) = \sum_{J_x, J_y} \omega_{J_x, J_y} e^{i\mathbf{K} \cdot \mathbf{X}} \quad (17)$$

Capital letters $(\mathbf{X}, \mathbf{K}, J_x, J_y)$ denote Lagrangian coordinates, and lower-case letters denote Eulerian ones. The transform of equation (8) gives the nonlinear mode coupling equation,

$$\begin{aligned} \frac{d\omega_{J_x, J_y}}{dT} &= \sum_{J'_x, J'_y} \omega_{J'_x, J'_y} \omega_{J_x - J'_x, J_y - J'_y} \frac{\hat{\mathbf{z}} \cdot [\mathbf{k}(\mathbf{K} - \mathbf{K}', T) \times \mathbf{k}(\mathbf{K}', T)]}{|\mathbf{k}(\mathbf{K}', T)|^2} \quad \text{in terms of which} \\ &= \sum_{J'_x, J'_y} \omega_{J'_x, J'_y} \omega_{J_x - J'_x, J_y - J'_y} \frac{\hat{\mathbf{z}} \cdot [\mathbf{K} \times \mathbf{K}']}{|\mathbf{k}(\mathbf{K}', T)|^2} \quad (18) \end{aligned}$$

where \mathbf{K}' is related to (J'_x, J'_y) via the analog of equation (16), and

$$\mathbf{k}(\mathbf{K}, T) \equiv \mathbf{K} + qT K_y \hat{\mathbf{x}} \quad (19)$$

is the wavevector with respect to \mathbf{x} . Equivalently, since a single mode has the spatial dependence

$$\exp(i\mathbf{K} \cdot \mathbf{X}) = \exp(i\mathbf{k}(\mathbf{K}, T) \cdot \mathbf{x}) \quad (20)$$

the Fourier transform of $\nabla \equiv (\partial_x, \partial_y)$ is obtained by making the substitution $\nabla \rightarrow i\mathbf{k}(\mathbf{K}, T)$. Hence equation (18) can be read directly from equation (8) after replacing the Fourier transform of \mathbf{u} with $(-i/k^2)\hat{\mathbf{z}} \times \mathbf{k}$ times the Fourier transform of ω (eq. [9]).

4. LINEAR EVOLUTION

The linearized equation of motion is $\partial\omega/\partial T = 0$, which has the general solution is

$$\omega = f(X, Y) = f(x, y + qtx \bmod L_y) \quad (21)$$

for any function f . A single vorticity wave can be written as

$$\omega = \bar{\omega} \cos(\bar{\mathbf{K}} \cdot \mathbf{X}) = \bar{\omega} \cos(\mathbf{k}(\bar{\mathbf{K}}, T) \cdot \mathbf{x}) \quad (22)$$

where $\bar{\omega}$ and $\bar{\mathbf{K}}$ are constants. The velocity fluctuation due to this wave is

$$\mathbf{u} = \hat{\mathbf{z}} \times \nabla \nabla^{-2} \omega \quad (23)$$

$$= \frac{\hat{\mathbf{z}} \times \mathbf{k}(\bar{\mathbf{K}}, T)}{|\mathbf{k}(\bar{\mathbf{K}}, T)|^2} \bar{\omega} \sin(\bar{\mathbf{K}} \cdot \mathbf{X}) \quad (24)$$

$$= \frac{(-\bar{K}_y, \bar{K}_x + qT\bar{K}_y)}{(\bar{K}_x + qT\bar{K}_y)^2 + \bar{K}_y^2} \bar{\omega} \sin(\bar{\mathbf{K}} \cdot \mathbf{X}) \quad (25)$$

the amplitude of which depends explicitly on T .

Equation (22) is not only a solution of the linearized equation of motion, but it is an exact solution of the nonlinear equation as well: the nonlinear term $\mathbf{u} \cdot \nabla \omega$ vanishes for a single wave because of incompressibility.

4.1. Axisymmetric, Swinging, and Radial Waves

Axisymmetric waves have $k_y = K_y = 0$: their phasefronts are aligned with the y -axis, which corresponds to the azimuthal direction in a Keplerian disk. See Figure 1. Axisymmetric waves are independent of time not only in shearing coordinates, but in unsheared ones as well. “Swinging waves” have $K_y \neq 0$. At early times ($T \rightarrow -\infty$), they are leading waves: the ratio $k_x/k_y \rightarrow -\infty$, so their phasefronts, though nearly axisymmetric, are tilted slightly into the first and third quadrants of the $x - y$ plane. As time evolves, the phasefronts swing first through the radial direction—parallel to the x -axis—and then, as $T \rightarrow +\infty$ they approach re-alignment with the azimuthal direction as a highly trailing wave. They are exactly radial at time

$$T_{\text{rad}}(\mathbf{K}) \equiv -\frac{K_x}{qK_y} \quad (26)$$

$$k_x = K_y q(T - T_{\text{rad}}) \quad (27)$$

We refer to a swinging wave at time T_{rad} as a “radial” wave, since its phasefronts are then aligned with the radial direction.

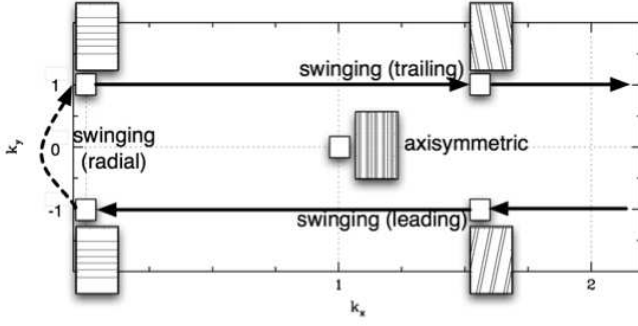


FIG. 1.— **Linear Evolution in k -space:** Only the half of k -space with $k_x > 0$ is plotted, the other half being redundant because a mode with wavevector $-\mathbf{k}$ is the complex conjugate of a mode with wavevector \mathbf{k} . Two modes are shown. The axisymmetric mode is the white square at $(k_x, k_y) = (1, 0)$; it does not move in k -space. The nearby rectangle depicts its contours of constant vorticity in $x-y$ space, and shows phasefronts aligned with the background shear, parallel to y . The second mode is a swinging mode. It evolves in time from the lower-right corner to the upper-right one. Rectangles again depict phasefronts at the corresponding positions in k -space. The dashed arrow at $k_x = 0$ can be thought of as an instantaneous jump in k_y : as a mode with $(k_x, k_y) = (0, -1)$ continues off the plot to negative k_x , its complex conjugate appears at $(0, 1)$.

4.2. Numerical Simulation: a Single Swinging Wave

Figure 2 shows the evolution of u_x and u_y of a swinging wave. The points show the output from the pseudospectral code described in the Appendix, and the curves through the points are given by equation (25). See the Figure's caption for details. Figure 3 shows contours of constant vorticity at three times in this simulation.

5. NONLINEAR EVOLUTION

The nonlinear coupling coefficient between two modes is time-dependent (eq. [18]), which at first sight makes the mode coupling problem look forbidding. But the situation is not quite so dire. The coupling coefficient depends on time only through its denominator

$$|\mathbf{k}(\mathbf{K}', T)|^2 = K_y'^2 (1 + q^2(T - T_{\text{rad}}(\mathbf{K}'))^2) , \quad (28)$$

which is smallest at the time when either of the modes has radial phasefronts ($k_x = 0$). At much earlier or later times the coupling $\propto T^{-2}$. Therefore integrated over time, most of the coupling occurs around the time that $k_x = 0$. Because mode couplings occur at essentially discrete times, the analysis is greatly simplified, as we presently show.

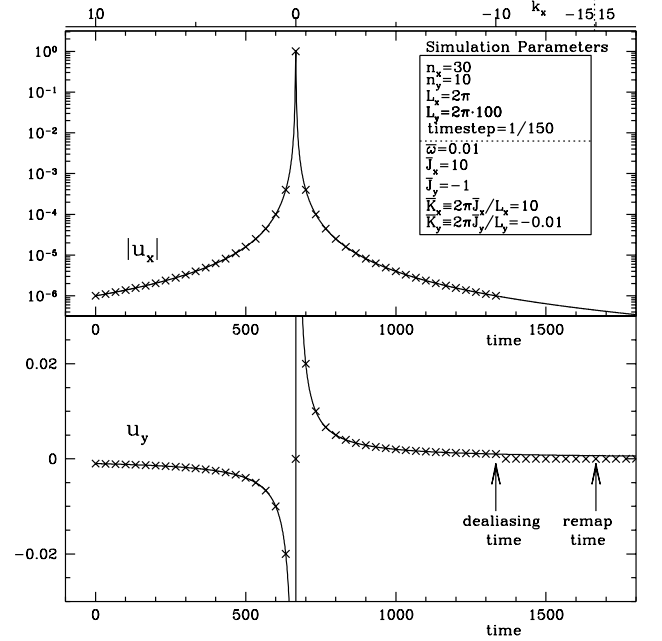


FIG. 2.— **Evolution of a Single Swinging Wave:** At $T = 0$, a vorticity wave (eq. [22]) is initialized with parameters as shown in the figure inset. J_x is the value of $J_x \equiv K_x L_x / 2\pi$ of the only non-zero mode; and similarly for J_y ; n_x, n_y are the number of grid-points in the simulation, and time is measured in units of Ω_0^{-1} . Points show output from pseudospectral code, properly normalized, i.e., they show $2\text{Im}(\mathbf{u}_{10, -1})$, where \mathbf{u}_{J_x, J_y} is the Fourier transform (as in eq. [15]). Lines through the points show the amplitude of equation (25): $\bar{\omega} \bar{K}_y / k^2$ in the top panel and $\bar{\omega} k_x / k^2$ in the bottom. At time $T_{\text{rad}} = -\bar{K}_x / q \bar{K}_y = 667$, phasefronts cross through the radial direction. In the pseudospectral code, dealiasing with the 2/3 rule sets $\mathbf{u}_{10, -1}$ to zero when this mode has $|k_x| > n_x/3 = 10$ (eq. [A21]). This occurs at time $20/q|\bar{K}_y| = 1333$. At a later time, when $|k_x| = n_x/2 = 15$ (which occurs at time $25/q|\bar{K}_y| = 1667$) the k_x of this mode is mapped from $k_x = -15$ to $k_x = 15$ via the modulus function in equation (A17). So this mode once again becomes a leading mode. However, since the amplitude of this mode was set to zero by dealiasing, it remains equal to zero.

5.1. Swinging Waves and a Single Axisymmetric Wave

To begin our investigation of the nonlinear coupling between waves, we consider the evolution of small swinging waves in the presence of a much larger axisymmetric wave. We set

$$\omega = 2\omega_{1,0} \cos(X) + \omega_{\text{swing}}(\mathbf{X}, T) , \quad (29)$$

with $|\omega_{\text{swing}}| \ll |\omega_{1,0}| \ll q$, and $\omega_{1,0}$ a real-valued constant; the factor of 2 multiplying $\omega_{1,0}$ has been inserted for consistency with equation (15). We have chosen the length unit so that the axisymmetric mode has $K_x = 1$.

Substituting equation (29) into equation (8) gives

$$\frac{\partial \omega_{\text{swing}}}{\partial T} = -2\omega_{1,0} \sin(X) (\nabla^{-2} + 1) \partial_y \omega_{\text{swing}} , \quad (30)$$

after dropping $\mathbf{u}_{\text{swing}} \cdot \nabla \omega_{\text{swing}}$.

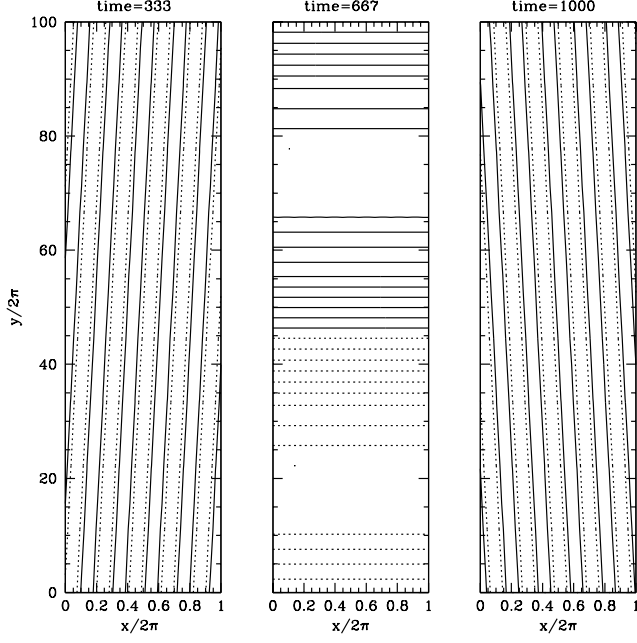


FIG. 3.— **Evolution of a Single Swinging Wave:** Contours of constant vorticity at three times from the simulation described in Figure 2, showing, respectively, leading, radial, and trailing phase-fronts.

Equation (30) is linear in ω_{swing} , with a spatially variable coefficient, $\sin(X)$. A Fourier mode of ω_{swing} with wavevector (K_x, K_y) couples with $\sin(X)$ to produce two modes with wavevectors $(K_x \pm 1, K_y)$. Hence a solution of equation (30) is⁴

$$\omega_{\text{swing}} = \sum_{J_x=-\infty}^{\infty} 2\omega_{J_x}(T) \cos(J_x X - \bar{K}_y Y). \quad (31)$$

Since we take K_y of the swinging modes as fixed (with $K_y = -\bar{K}_y < 0$), we suppress the corresponding subscript J_y from ω_{J_x, J_y} ; mode amplitudes with a single subscript all label modes with the same $J_y \neq 0$, where $K_y = 2\pi J_y / L_y$. Substituting the above ω_{swing} into equation (30),

$$\frac{d\omega_{J_x}}{dT} = -\bar{K}_y \omega_{1,0} \left(\frac{\omega_{J_x-1}}{k_{J_x-1}^2} - \frac{\omega_{J_x+1}}{k_{J_x+1}^2} \right), \quad (32)$$

where

$$k_{J_x}^2 \equiv (J_x - qT\bar{K}_y)^2 + \bar{K}_y^2 \quad (33)$$

$$= \bar{K}_y^2 (1 + q^2(T - T_{\text{rad}, J_x})^2), \quad (34)$$

and

$$T_{\text{rad}, J_x} \equiv T_{\text{rad}}(J_x, -\bar{K}_y) = \frac{J_x}{q\bar{K}_y} \quad (35)$$

(eq. [26]). In writing equation (32), we kept only the ∇^{-2} term from the right-hand side of equation (30). To include the full $\nabla^{-2} + 1$, one should replace the $k_{J_x \pm 1}^{-2}$ in equation (32) with $k_{J_x \pm 1}^{-2} - 1$; we show below that the omitted terms are small (eq. [46]). The ∇^{-2} term is due to the advection of the axisymmetric wave by the swinging ones, i.e., it

⁴ This is clearly not the complete solution. But each “chain” of modes represented by equation (31), with fixed \bar{K}_y and $-\infty < J_x < \infty$, evolves independently of others. For the complete solution, one should also sum over different K_y , and include chains whose $k_x(T=0)$ are not integer multiples of the axisymmetric mode’s K_x ; these chains are also described by equation (31), except that their time origin (when $K_x = k_x$) is offset from $T = 0$. Note also that for simplicity we have not included arbitrary phases in the arguments of the cosines (i.e., we take mode amplitudes to be real-valued). It is trivial to include phases; we do so in §5.4.

is $-\mathbf{u}_{\text{swing}} \cdot \nabla \omega_{1,0} \cos(X)$. The dropped term represents advection of the swinging waves by the axisymmetric one.

If $\bar{K}_y \ll 1$, then the squared wavevectors that appear in the denominator in equation (32) reach very small values when the corresponding mode is radial. At this time, the mode strongly influences its two neighboring modes. We shall see that we can often approximate the interaction between different swinging waves as occurring solely when one of the waves passes through the radial direction.

As an example, at $T = 0$ we initialize ω_{swing} with a single leading wave:

$$\omega_{\text{swing}}(\mathbf{X}, T = 0) = 2\epsilon \cos(X - \bar{K}_y Y), \quad (36)$$

i.e., with $\omega_1 = \epsilon$, and $\omega_{J_x} = 0$ for $J_x \neq 1$. We choose

$$0 < \bar{K}_y \ll 1 \quad (37)$$

$$\epsilon \ll |\omega_{1,0}|, \quad (38)$$

and follow the evolution governed by equation (32). See Figure 4.

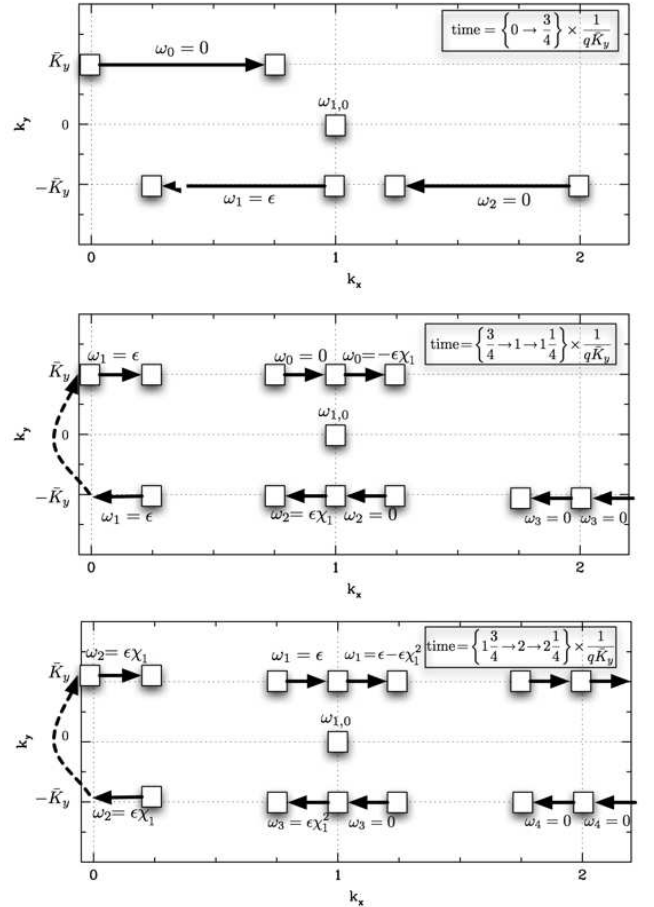


FIG. 4.— **Early-Time Evolution in k -space:** The top panel shows four modes between the times 0 and $3/4q\bar{K}_y$. For example, the square at $(k_x, k_y) = (1, -\bar{K}_y)$ represents ω_1 at time $T = 0$; the connecting arrow shows this mode’s trajectory in k -space until time $3/4q\bar{K}_y$. The middle panel continues the evolution through time $T_{\text{rad},1} = 1/q\bar{K}_y$, when ω_1 is radial, and ω_0 and ω_2 interact strongly with the radial and axisymmetric modes. At this time, ω_2 changes from 0 to $\epsilon\chi_1$, and ω_0 changes from 0 to $-\epsilon\chi_1$. The bottom panel follows the evolution through time $T_{\text{rad},2} = 2/q\bar{K}_y$.

At first, the only non-zero swinging mode is ω_1 . This mode influences only two others: ω_2 and ω_0 . So at early times, ω_2 approximately satisfies

$$\frac{d\omega_2}{dT} = -\bar{K}_y \omega_{1,0} \frac{\omega_1}{k_1^2} \quad (39)$$

$$= -\frac{\omega_{1,0}}{\bar{K}_y} \frac{\omega_1}{1 + q^2(T - T_{rad,1})^2} \quad (40)$$

Integrating this from time $T = 0$ through $T_{rad,1} = 1/(q\bar{K}_y)$, we see that most of the integral comes from within a time $\sim 1/q$ of $T_{rad,1}$, when the phasefronts of ω_1 are within around $\pm 45^\circ$ to the radial direction. So we can extend the integration to the domain $-\infty < T < \infty$ to obtain shortly after time $T_{rad,1}$, i.e. at time $\sim (1 + q\bar{K}_y)T_{rad,1}$,

$$\omega_2 = \omega_1 \chi_1 = \epsilon \chi_1 \quad (41)$$

where

$$\chi_1 \equiv -\frac{\pi}{q\bar{K}_y} \omega_{1,0}, \quad (42)$$

is the dimensionless parameter that controls the linear evolution of ω_{swing} . The behavior of ω_0 at time $T_{rad,1}$ is similar to ω_2 , with $\omega_0 = -\epsilon \chi_1$ shortly after $T_{rad,1}$.

In the top panel of Figure 4, the modes initially evolve linearly, with constant amplitude and $k_x = K_x - qTK_y$. Before time $T_{rad,1}$, both ω_1 and ω_2 are leading modes (their $k_x/k_y < 0$), and ω_0 is trailing. But when ω_1 becomes radial and its $k_x = 0$, the amplitudes of modes ω_0 and ω_2 change abruptly (Figure 4, middle panel). Qualitatively, the velocity field of the ω_1 mode when it becomes radial is $\mathbf{u}^{rad} = -\hat{x}(2\epsilon/\bar{K}_y)\sin(\bar{K}_y y)$ (eq. [25]). Since it takes a time $\sim 1/q$ to swing through the radial direction, the corresponding displacement field is $\boldsymbol{\xi}^{rad} \sim \mathbf{u}^{rad}/q$, which advects the axisymmetric mode, changing it by an amount $-\boldsymbol{\xi}^{rad} \cdot \nabla 2\omega_{1,0} \cos(X) \sim -2\epsilon(\omega_{1,0}/q\bar{K}_y)(\cos(x - \bar{K}_y y) - \cos(x + \bar{K}_y y))$. Hence the ω_2 mode, which has the spatial dependence $\cos(x - \bar{K}_y y)$ at this time, changes its amplitude by $\sim -\epsilon(\omega_{1,0}/q\bar{K}_y)$, as in equation (41); similarly, ω_0 is changed by an equal and opposite amount.

After time $T_{rad,1}$, the next time of interest is $T_{rad,2} = 2/q\bar{K}_y$, when the ω_2 mode is radial with $\omega_2 = \epsilon \chi_1$ (Figure 4, bottom panel). The evolution of ω_3 around this time is given by the analog of equation (39), i.e., $d\omega_3/dT = -\bar{K}_y \omega_{1,0} \omega_2/k_1^2$. Integrating through time $T_{rad,2}$ yields $\omega_3 = \omega_2 \chi_1 = \epsilon \chi_1^2$ shortly after $T_{rad,2}$. Similarly, ω_1 changes by an equal and opposite amount.

Extrapolating to later times, it is clear that the amplitude of the mode that crosses through the radial direction is

$$\omega_{J_x} = \epsilon \chi_1^{J_x - 1} \text{ at time } T_{rad,J_x} = \frac{J_x}{q\bar{K}_y}. \quad (43)$$

As time progresses, the amplitudes of the radial waves grow exponentially if $|\chi_1| > 1$; conversely, they decay exponentially if $|\chi_1| < 1$. At marginal stability,

$$\kappa \equiv \bar{K}_y \Big|_{\text{marginal stability}} = \frac{\pi|\omega_{1,0}|}{q}. \quad (44)$$

(If we do not set $K_x = 1$ for the axisymmetric mode then $\kappa = \pi|K_{x,axi}\omega_{1,0}/q|$). Since $|\chi_1| = \kappa/\bar{K}_y$, equation (43) shows

$$|\omega_{J_x}| \propto \exp(|\omega_{1,0}|T_{rad,J_x}\pi(\bar{K}_y/\kappa)\ln(\kappa/\bar{K}_y)), \quad (45)$$

and hence the growth rate is very small both when $\bar{K}_y \rightarrow \kappa$ and when $\bar{K}_y \rightarrow 0$; it is fastest for $\bar{K}_y = \kappa/e = 0.368\kappa$.

5.2. Numerical Simulation

Figures 5 and 6 show results from two pseudospectral simulations. At $T = 0$, the vorticity field was given by equations (29) and (36), i.e., $\omega(T = 0) = 2\omega_{1,0} \cos(X) + 2\epsilon \cos(X - \bar{K}_y Y)$. One of the simulations had $\chi_1 = -1.1$, and the other had $\chi_1 = -0.9$. In Figure 5, we plot the amplitudes of the first eight modes that pass through the radial direction in the $\chi_1 = -1.1$ simulation. Most of the time the amplitudes remain constant. Only at times T_{rad,J_x} do the amplitudes of modes $J_x \pm 1$ change abruptly; see also Figure 4.

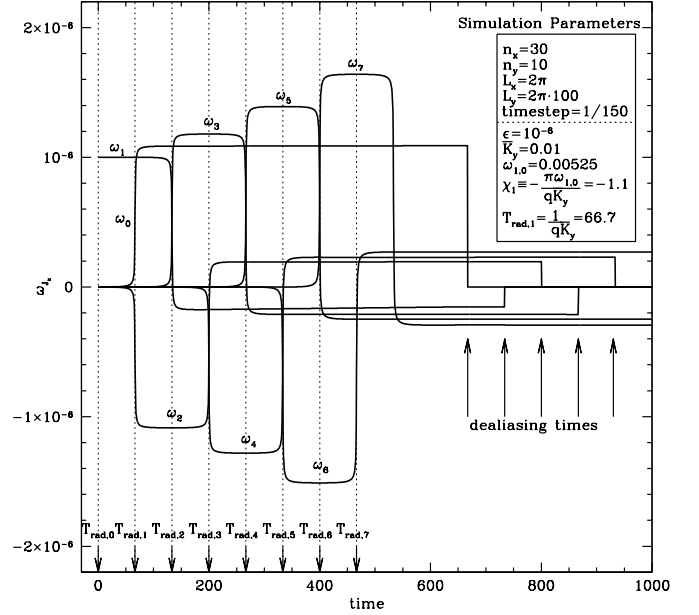


FIG. 5.— **Swinging Waves in the Presence of a Large Axisymmetric Wave:** Pseudospectral simulation of the fully nonlinear equations of motion. The vorticity field was initially $\omega(T = 0) = 2\omega_{1,0} \cos(X) + 2\epsilon \cos(X - \bar{K}_y Y)$ (eqs. [29] and [36]); parameters are listed in inset. Curves show $\omega_{J_x} = \text{Re}(\omega_{J_x, -1})$. Dealiasing is described in §A.

The points in Figure 6 show the amplitudes of radial modes at each time that a mode is precisely radial. The line through the points is the theoretical prediction. (Of course, only at the discrete times T_{rad,J_x} , for integer J_x , is there a radial mode; the theoretical prediction is plotted as a line for clarity.) The theoretical prediction is given by equation (43), but with a slightly modified χ_1 . In particular, in deriving equation (43), we made two approximations that are applicable as $\bar{K}_y \rightarrow 0$; we shall now include the $O(\bar{K}_y)$ corrections. First, we integrated equation (39) from $-\infty$ to ∞ , whereas we should have integrated from ~ 0 to $\sim 2/q\bar{K}_y$; second, instead of ω_1/k_1^2 in equation (39), we should have $\omega_1(1/k_1^2 - 1)$. Both corrections can be absorbed into a redefinition of the dimensionless parameter,

$$\tilde{\chi}_1 \equiv \chi_1 \cdot \left(1 - \frac{4}{\pi} \bar{K}_y\right); \quad (46)$$

$\tilde{\chi}_1$ should be inserted in equation (43) in place of χ_1 . As long as $\bar{K}_y \ll 1$, this correction is small. Nonetheless, accumulated corrections can be substantial if $\tilde{\chi}_1$ is exponentiated many times. For example, in the top panel of

Figure 6, using $\chi_1 = -1.1$ instead of $\tilde{\chi}_1 = -1.086$ would overpredict the amplitude of the last plotted point by a factor of 2.

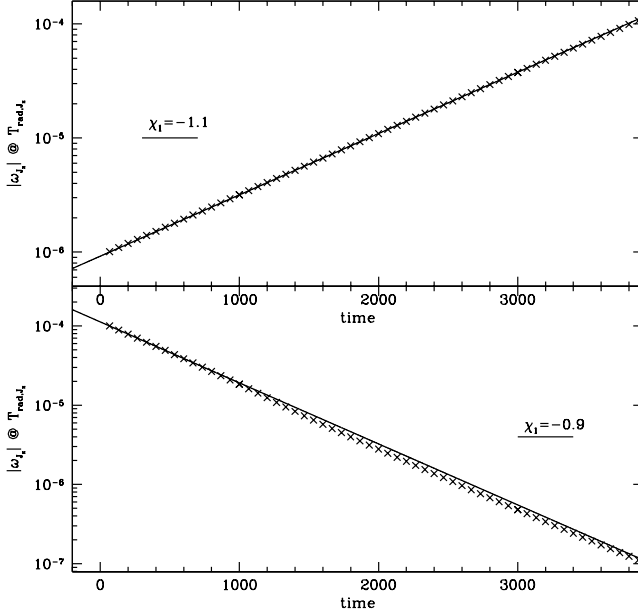


FIG. 6.— **Amplitudes of Radial Modes:** Points in the top panel show results from the pseudospectral simulation described in Figure 5, extended to later times. Each point shows the amplitude of the mode that is radial at that time. The line through the points shows the theoretical prediction $\epsilon|\tilde{\chi}_1|^{q\bar{K}_y T^{-1}}$, as in eq. [43], but with $\tilde{\chi}_1 = -1.086$ in place of $\chi_1 = -1.1$; see eq. [46]. Bottom panel shows results from a simulation identical to top panel's, except with $\omega_{1,0} = 0.0043 \Rightarrow \chi_1 = -0.9$ and $\epsilon = 10^{-4}$. Note that the last point in both panels has $J_x = 58$, even though the simulations only have $n_x/2 = 15$ modes in the x -direction: modes are “recycled” by the remapping that is performed by the modulus operator (eq. [A17]).

5.3. Quasi-Eulerian Notation

Analysis of the coupling between Fourier modes is simpler when a quasi-Eulerian notation is used; we introduce this notation here. Instead of ω_{j_x, j_y} , where the subscripts label the mode's Lagrangian wavevector \mathbf{K} , we label a mode's amplitude

$$\omega^{j_x, j_y} \quad (47)$$

when the mode's Eulerian wavevector $\mathbf{k}(\mathbf{K}, T)$ satisfies

$$k_x = \frac{2\pi}{L_x} j_x \quad \text{and} \quad k_y = \frac{2\pi}{L_y} j_y, \quad (48)$$

where j_x and j_y are any integers. Since k_x is time dependent, equation (48) only applies at discrete times. But we shall also label a mode's amplitude with ω^{j_x, j_y} at times shortly before, and shortly after, its \mathbf{k} satisfies equation (48); see Figure 7. (To be more precise, one might say that a mode whose k_x increases in time has its label switched from ω^{j_x, j_y} to ω^{j_x+1, j_y} when its k_x passes through $(2\pi/L_x)(j_x + 1/2)$; but this increased precision is unnecessary.)

⁵ We are assuming that the amplitude of a swinging mode hardly changes as it crosses through the radial direction, i.e., for $-\bar{K}_y \lesssim k_x \lesssim \bar{K}_y$. This assumption follows from the requirement that \bar{K}_y be much smaller than the typical k_x of ω_{axi} .

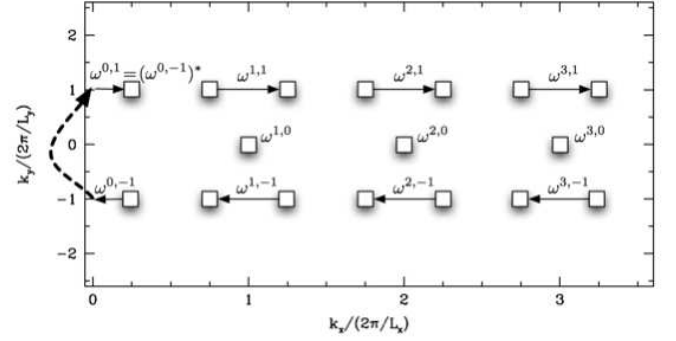


FIG. 7.— **Quasi-Eulerian Notation:** Squares represent the wavevectors \mathbf{k} of a number of modes at two successive times, $T = T_{\text{rad}} - 1/4q\bar{K}_y$ and $T = T_{\text{rad}} + 1/4q\bar{K}_y$, where T_{rad} is the radial time of the mode labelled $\omega^{0,-1}$ in the Figure. Modes are labelled by superscripts j_x, j_y representing the nearest k_x, k_y . Axisymmetric modes have $k_y = 0$. Because their \mathbf{k} does not evolve, their quasi-Eulerian indices are the same as their Lagrangian ones.

5.4. Many Axisymmetric Waves

We have shown above that a single axisymmetric wave is unstable to interactions with swinging waves whose \bar{K}_y are sufficiently small that $|\chi_1| > 1$. In the present subsection, we show how to generalize this result to consider many axisymmetric waves, and so re-derive standard results regarding the instability of shear flows with inflection points in the limit that $|\omega| \ll q$ and that the vorticity is elongated in the streamwise direction.

We generalize equation (29) to

$$\omega = \omega_{\text{axi}}(x) + \omega_{\text{swing}}(\mathbf{X}, T), \quad (49)$$

where ω_{axi} is an arbitrary axisymmetric function,

$$\omega_{\text{axi}}(x) = \sum_{j_x=-\infty}^{\infty} \omega^{j_x, 0} \exp(ij_x x), \quad (50)$$

with $\omega^{j_x, 0}$ arbitrary constants and $L_x = 2\pi$. We seek solutions to linear order in ω_{swing} . No new values of k_y can be generated by mode couplings because swinging modes must couple with axisymmetric modes, which have $k_y = 0$. We take ω_{swing} to have $k_y = \pm\bar{K}_y$, where $\bar{K}_y > 0$, and \bar{K}_y is much smaller than the typical k_x of ω_{axi} . Equation (18) gives the equations of motion in Lagrangian notation. We switch to quasi-Eulerian notation by replacing subscripts with superscripts, and capitalized indices with lower-case ones. As in §5.1, for small \bar{K}_y most of the coupling between modes occurs when one of the modes is radial, i.e., when the term $|\mathbf{k}(\mathbf{K}', T)|^2$ in the denominator of equation (18) nearly vanishes. So we take $\omega_{j_x', j_y'}$ in this equation to be the nearly radial mode $\omega^{0, \pm 1}$ (setting $L_y = 2\pi/\bar{K}_y$ so that $j_y = \pm 1$), and, from equations (18) and (27),

$$\frac{d\omega^{j_x, -1}}{dT} = -\omega^{0, -1} \omega^{j_x, 0} \frac{j_x}{\bar{K}_y} \frac{1}{1 + q^2(T - T_{\text{rad}})^2}, \quad (51)$$

where T_{rad} is the time when $\omega^{0, -1}$ is radial. Equation (51) generalizes the first term in equation (32) to arbitrary j_x and complex mode amplitudes. We integrate from

$T = -\infty$ to $+\infty$ because most of the integral comes from within a time $\sim 1/q$ of T_{rad} .⁵ The change in $\omega^{j_x, -1}$ at this time is

$$\Delta\omega^{j_x, -1} = \chi_{j_x} \omega^{0, -1}, \quad (52)$$

where

$$\chi_{j_x} \equiv -\frac{\pi}{q\bar{K}_y} j_x \omega^{j_x, 0}. \quad (53)$$

The mode that is labelled $\omega^{0, -1}$ at time T_{rad} was, at the earlier time $T_{\text{rad}} - 1/q\bar{K}_y$, labelled $\omega^{1, -1}$. At that earlier time, its change due to the then-radial mode was $\chi_1 \omega^{0, -1}|_{T_{\text{rad}} - 1/q\bar{K}_y}$. Extrapolating to still earlier times, we conclude

$$\omega^{0, -1} \Big|_{T=J/q\bar{K}_y} = \sum_{j'_x=1}^{\infty} \chi_{j'_x} \omega^{0, -1} \Big|_{T=(J-j'_x)/q\bar{K}_y}, \quad (54)$$

where J is an integer. Solutions of this difference equation have the form

$$\omega^{0, -1} \Big|_{T=J/q\bar{K}_y} = \text{constant} \times z^J, \quad (55)$$

with z determined by the roots of the characteristic equation

$$1 = \sum_{j'_x=1}^{\infty} \chi_{j'_x} z^{-j'_x}. \quad (56)$$

This is the dispersion relation; unstable modes have $|z| > 1$. The eigenfunction is, generalizing equation (54),⁶

$$\omega^{j_x, -1} \Big|_{T=J/q\bar{K}_y} = \sum_{j'_x=j_x+1}^{\infty} \chi_{j'_x} \omega^{0, -1} \Big|_{T=(J+j_x-j'_x)/q\bar{K}_y} \quad (57)$$

$$= \text{constant} \times z^J \sum_{j'_x=j_x+1}^{\infty} \chi_{j'_x} z^{j_x-j'_x} \quad (58)$$

At marginal stability,

$$z = e^{-i\beta}, \quad (59)$$

for a real-valued β , and the dispersion relation (eq. [56]) is

$$1 = \frac{1}{2q\bar{K}_y} \int_{-\infty}^{\infty} dx \frac{d\omega_{\text{axi}}/dx}{x - \beta} + i \frac{\pi}{2q\bar{K}_y} \frac{d\omega_{\text{axi}}}{dx} \Big|_{x=\beta}, \quad (60)$$

after changing the sum over j'_x to an integral, and extending the box-size L_x to ∞ . The imaginary part of the dispersion relation shows that β must be chosen at a zero of $d\omega_{\text{axi}}/dx$; the real part gives the marginally stable \bar{K}_y :

$$\kappa \equiv \bar{K}_y \Big|_{\text{marginal stability}} \quad (61)$$

$$= \frac{1}{2q} \int_{-\infty}^{\infty} dx \frac{d\omega_{\text{axi}}/dx}{x - \beta} \Big|_{\beta = \text{zero of } d\omega_{\text{axi}}/dx} \quad (62)$$

In §5.1, we had $\omega_{\text{axi}} = 2\omega_{1,0} \cos x$; inserting this into the above integral gives $\kappa = \pi|\omega_{1,0}|/q$, as in equation (44). For an arbitrary profile of ω_{axi} , if the right-hand side of equation (62) is negative for each β that is a zero of $d\omega_{\text{axi}}/dx$, then that profile is stable to all small perturbations. Conversely, if the right-hand side is positive for any β , then there are unstable modes with $\bar{K}_y < \kappa$. This is the general

⁶ To be more precise, the left-hand side of equation (57) should be evaluated not precisely at time $J/q\bar{K}_y$, but slightly sooner—before this swinging mode has been altered by the radial mode. But this distinction is unimportant when the typical j_x of ω_{axi} is much larger than unity, in which case j_x may be treated as a continuous variable.

⁷ Although ω_{swing} is cut off at $|x| \gtrsim \alpha$, $u_{x, \text{swing}}$ extends further, to $|x| \sim \pm 1/\bar{K}_y$; see §6.

stability criterion. Equation (62) is derived by Gill (1965), although using an entirely different method. That shear flows can become unstable only when the velocity field has an inflection point (i.e., when $d\omega_{\text{axi}}/dx = 0$) is known as Rayleigh's inflection point theorem (Drazin & Reid 2004).

For an unstable mode,

$$z = e^{\alpha - i\beta}, \quad \alpha > 0, \quad (63)$$

and the dispersion relation is

$$1 = \frac{1}{2q\bar{K}_y} \int_{-\infty}^{\infty} dx \frac{d\omega_{\text{axi}}/dx}{x - \beta - i\alpha}, \quad (64)$$

which reduces to equation (60) as $\alpha \rightarrow 0$.

Since the eigenfunction is a convolution in Fourier space (eq. [58]), it is simply expressed in real-space:

$$\omega_{\text{swing}} = e^{\alpha q T \bar{K}_y} \frac{d\omega_{\text{axi}}}{dx} \cdot \text{Re} \left\{ \text{const} \frac{e^{-i\bar{K}_y(y + \beta q T \bar{K}_y)}}{1 + i(x - \beta)/\alpha} \right\}, \quad (65)$$

where the constant is an arbitrary complex number, and we have set $J = qT\bar{K}_y$. A more transparent way of writing the eigenfunction is to combine it with ω_{axi}

$$\omega = \omega_{\text{axi}} + \omega_{\text{swing}} = \omega_{\text{axi}}(x + \xi(x, y, T)), \quad (66)$$

where the displacement field ξ is given by

$$\xi(x, y, T) = \xi(0, y_0, 0) \times e^{\alpha q T \bar{K}_y} \text{Re} \left\{ \frac{1}{1 + ix/\alpha} e^{-i\bar{K}_y(y - y_0)} \right\}; \quad (67)$$

y_0 is an arbitrary constant, and we have set $\beta = 0$, which can be done by changing the origin of the x -axis.

The exponential growth rate is $\gamma = \alpha q \bar{K}_y$. Note that α has the physical interpretation that fluid at $x = \pm\alpha$ is advected by the background flow $-qx\hat{\mathbf{y}}$ a distance $1/\bar{K}_y$ in the growth time $1/\gamma$. Fluid at $|x| \gg \alpha$ is advected many wavelengths in a growth time; this phase mixing implies that the eigenfunction is cut off at $|x| \gg \alpha$.⁷

5.5. Numerical Simulation

We use the pseudospectral code to simulate the equations of motion with ω_{axi} given by a Gaussian profile,

$$\omega_{\text{axi}}(x) = -\bar{\omega} \exp(-x^2/s^2), \quad (68)$$

with $s\bar{K}_y \ll 1$ and $\bar{\omega} > 0$. This profile is somewhat unrealistic because it does not integrate to zero. Hence it produces a velocity field u_y that is infinite in extent. Nonetheless, we show in §6.5 that profiles that do not integrate to zero behave similarly to those that do.

The marginally stable wavenumber is (eq. [62])

$$\kappa = \sqrt{\pi} \frac{\bar{\omega}}{qs}. \quad (69)$$

The imaginary and real parts of the dispersion relation (eq. [64]) imply

$$\beta = 0 \quad (70)$$

$$1 = \frac{\bar{\omega}}{q\bar{K}_y s^2} \int_{-\infty}^{\infty} dx \frac{x^2}{x^2 + \alpha^2} e^{-x^2/s^2} \quad (71)$$

$$= \frac{\kappa}{\bar{K}_y} \left(1 - \sqrt{\pi} \frac{\alpha}{s} e^{(\alpha/s)^2} \text{erfc}(\alpha/s) \right) \quad (72)$$

Solving the latter equation for α gives the exponential growth rate

$$\gamma = \alpha q \bar{K}_y = \bar{\omega} f\left(\frac{\bar{K}_y}{\kappa}\right) \quad (73)$$

where $f(\bar{K}_y/\kappa)$ is plotted in the top panel of Figure 8. The three points in that panel show results from numerical simulations; see caption for details. The fastest growing mode has $\bar{K}_y/\kappa = 0.299$ and growth rate = $0.435\bar{\omega}$. The bottom panel shows that when our assumption $s\bar{K}_y \ll 1$ is no longer valid, the growth rate differs from equation (73).

In Fourier-space, the eigenfunction at a fixed time is

$$\omega^{j_x, -1} = \text{constant} \times e^{-(sj_x/2)^2} \times \left(1 - \sqrt{\pi} \frac{\alpha}{s} e^{(\alpha/s + sj_x/2)^2} \text{erfc}(\alpha/s + sj_x/2)\right) \quad (74)$$

after changing the sum in equation (58) to an integral. In Figure 9, we show that this agrees with the output from a numerical simulation.

Figure 10 shows contours of constant ω at two times, and shows that theory agrees with simulation. At later times than those shown, the vorticity tends to wrap up into a vortex, with large spatial variations in ω . To simulate this with the pseudospectral code, we must introduce an explicit viscosity, which smooths out the variations in ω . But the highly nonlinear state can be simulated with no viscosity with a Lagrangian code; we shall do so in §6.3.

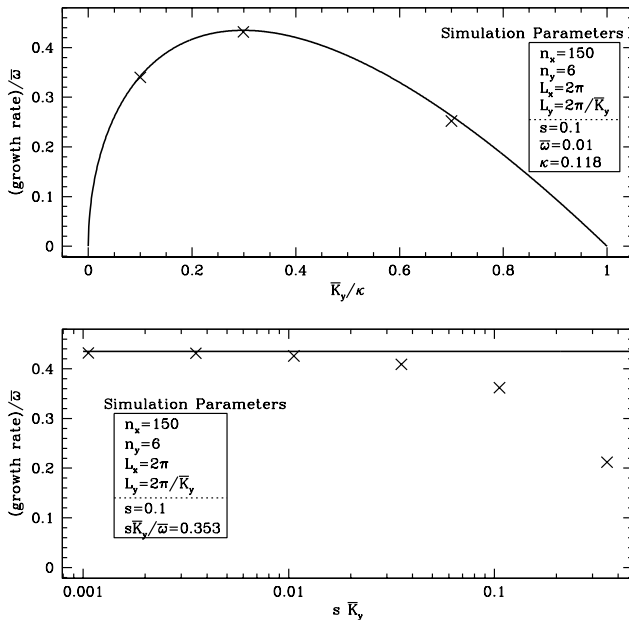


FIG. 8.— **Exponential Growth Rate:** Curve in top panel shows growth rate obtained by solving equation (72) for α/s with Mathematica. Points show results from three simulations with varying \bar{K}_y , but otherwise identical. In the simulations, ω_{axi} was initialized as $-\bar{\omega}(\exp(-x^2/s^2) - \sqrt{\pi}s/L_x)$, which differs from equation (68) by the addition of a constant term that eliminates the zero-frequency component. ω_{swing} was initialized as $\epsilon \cos(\bar{K}_y y)$, with $\epsilon = 10^{-6}$. The growth rate was extracted from each simulation by plotting the amplitudes of the radial modes versus time (as in Figure 6), and fitting with an exponential. For the fastest growing mode, $\bar{K}_y/\kappa = 0.299$. In the bottom panel, we show results from six simulations with fixed $\bar{K}_y/\kappa = 0.299 \Rightarrow s\bar{K}_y/\bar{\omega} = 0.353$, and fixed s , but varying \bar{K}_y and $\bar{\omega}$. Equation (73) predicts that the growth rate should be equal to $0.435\bar{\omega}$, independent of $s\bar{K}_y$. Numerical results (points in figure) agree with this prediction for $s\bar{K}_y \lesssim 0.01$. The theory leading to equation (73) is only applicable for $s\bar{K}_y \ll 1$.

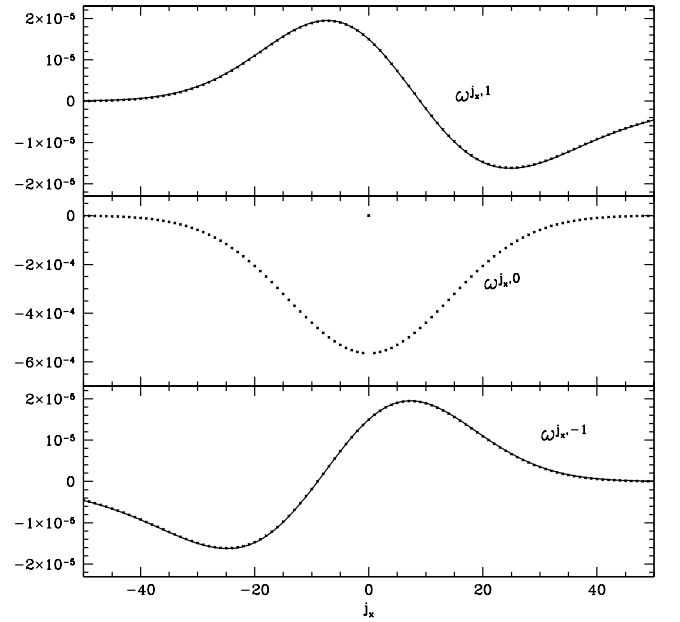


FIG. 9.— **Vorticity in Fourier-Space:** Points show output from the simulation described in Figure 8 that had $\bar{\omega} = 0.01$, $s = 0.1$, $\bar{K}_y/\kappa = 0.299$, and hence $\alpha = 0.082$. The vorticity shown was output at time $T = 1208$. Top and bottom panels depict the eigenfunction. By the reality condition $\omega^{j_x, 1} = (\omega^{-j_x, -1})^*$. The curve through the points in these two panels is equation (74), with the normalization chosen to fit the points. The agreement between theory and simulation is quite good. The middle panel simply reflects the initial ω_{axi} , i.e., it is the Fourier transform of equation (68) (with no $j_x = 0$ component, as described in Figure 8).

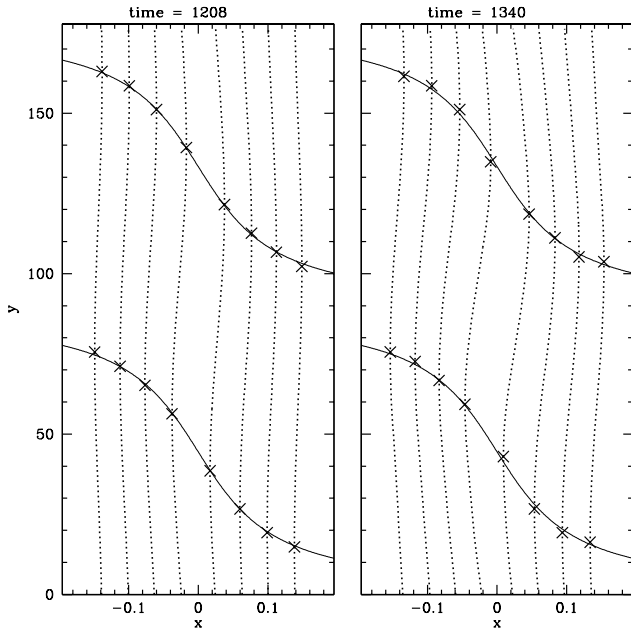


FIG. 10.— Contour Plots at Two Times: Dotted lines trace contours of constant $\omega = \omega_{\text{axi}} + \omega_{\text{swing}}$ from a simulation identical to the one described in Figure 9, but with $n_x = 600$ instead of 150. To compare with the theoretical prediction (eq. [65], or equivalently, eq. [67]), we plot two points on each contour where the contour’s x -position is extremal. From equation (67), the extrema should be at $y_{\text{ext}} = (\phi - \tan^{-1}(x/\alpha))/\bar{K}_y$, where $\phi = \pi/2$ and $3\pi/2$. We plot these two y_{ext} as solid lines, with $\alpha = 0.082$ (as obtained from Figure 8). The lines nearly go through the points, implying good agreement.

6. SHEAR INSTABILITY IN REAL SPACE

We seek a better understanding of the instability discussed in §5. The instability of shear flows with inflection points in the streamwise velocity field—or equivalently, with $d\omega_{\text{axi}}/dx = 0$ (eq. [62])—is well known (Drazin & Reid 2004). However, we have not found in the literature a simple yet quantitatively accurate explanation for why it occurs. Why are only certain shear flows unstable, and why only for sufficiently small wavenumbers? We give a dynamical explanation for a top-hat profile in §6.1, and an explanation based on momentum and energy considerations in §6.2. We also simulate the development of the instability into the highly nonlinear regime in §6.3. We generalize these results from a top-hat profile to an arbitrary one in §6.4, and present another simulation in §6.5.

6.1. Top-Hat Vorticity Profile

We consider in some detail the dynamics when the unperturbed ω is given by the top-hat profile

$$\omega_{\text{unp}} = \begin{cases} \mu & , \quad |x| < s \\ 0 & , \quad |x| > s \end{cases}, \quad (75)$$

where μ and s are constants, with $s > 0$. The total unperturbed vorticity is $-q + \omega_{\text{unp}}$, and we assume that $|\mu| \ll q$. The top-hat profile is perhaps the simplest profile that exhibits instability. It is not a realistic profile, both because real fluids are not discontinuous, and because it produces a u_y -field that is infinite in extent. But once the results

for the top-hat are in hand, it is trivial to extend them to profiles that do not suffer from these defects. We do so in §§6.4-6.5, where we show that more realistic profiles behave similarly to the top-hat.

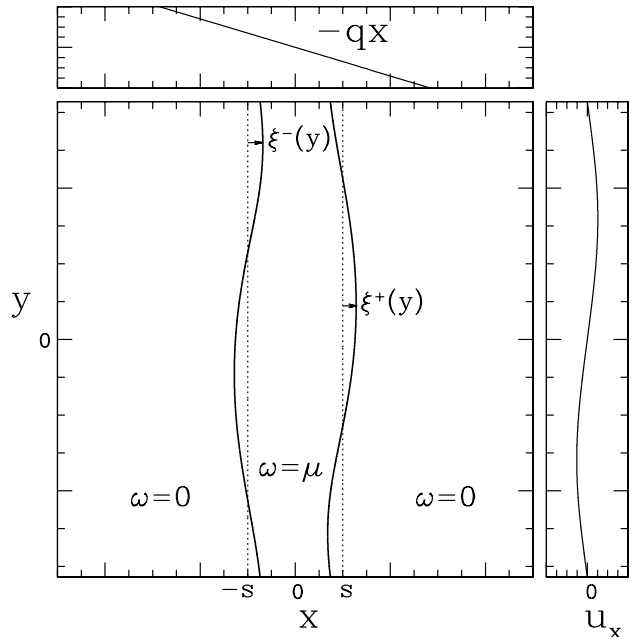


FIG. 11.— Perturbed Top-Hat Profile: Main panel shows contours of constant vorticity. Dotted lines are for the unperturbed profile (eq. [75]), and solid lines are perturbed. Top and right panels show the velocity fields that advect the contours. The top panel shows the amplitude of the background shear profile $-qx\hat{y}$, and the right one shows u_x as a function of y . As long as inequality (78) is satisfied, u_x can be taken to be independent of x . u_y is not depicted because advection in the y direction is dominated by the background shear. The data for this figure come from the simulation described in §6.3 at time=4000. This simulation has $\mu < 0$ and $|k_y| < |\mu|/qs$, so that instability results. Spatial and velocity axes are not to scale.

We perturb the top-hat by displacing the two contours at x_- and x_+ by $\xi^-(y, t)$ and $\xi^+(y, t)$, as in Figure 11, and seek equations of motion for the contours (“contour dynamics,” e.g., Pullin 1992). We can adopt this partially Lagrangian description as long as a contour does not fold back upon itself; otherwise, ξ becomes multiple-valued, and a fully Lagrangian or an Eulerian description would be preferable. Although tracking contours is simpler than the mode coupling method of earlier sections, mode coupling can readily be generalized to three dimensions, whereas contour dynamics cannot: by tracking the contours, we rely on the fact that ω is locally conserved, which is only true in two dimensions. We still assume that the dynamics occur in a box that is periodic in y with size L_y ; but we now assume L_x is sufficiently large that the boundary conditions in x are unimportant. (From eq. [81] below, it suffices to take $L_x \gg 1/k_y$ for all k_y .) We shall make use of Fourier transforms, but only in the y -dimension, with

$$\omega_{k_y}(x) \equiv \int_{-L_y/2}^{L_y/2} \omega(x, y) e^{-ik_y y} \frac{dy}{L_y} \quad (76)$$

$$\Rightarrow \omega(x, y) = \sum_{k_y} \omega_{k_y}(x) e^{ik_y y} \quad (77)$$

and similarly for $u_{x, k_y}(x)$, ξ_{k_y} etc., where $k_y = (2\pi/L_y)\times$

integer.

We shall see that instability can only occur when $|k_y|s < |\mu|/q \ll 1$; therefore we assume at the outset that perturbations are elongated in the streamwise direction,

$$|k_y|s \ll 1. \quad (78)$$

The contours are advected by the total velocity field $-qx\hat{y} + \mathbf{u}$ (eq. [8]), implying

$$(\partial_t \mp qs\partial_y)\xi^\pm = u_x, \quad (79)$$

after dropping the nonlinear terms $(-q\xi^\pm + u_y)\partial_y\xi^\pm$. In Fourier-space,

$$\left(\frac{d}{dt} \mp qsk_y\right)\xi_{k_y}^\pm = u_{x,k_y} \quad (80)$$

We need not distinguish the u_x that advects ξ^+ from the one that advects ξ^- , as we presently show.

To find u_{x,k_y} , we have $u_x = -\partial_y\nabla^{-2}\omega$ (eq. [9]), or

$$u_{x,k_y} = \frac{i}{2}\text{sgn}(k_y) \int \omega_{k_y}(x')e^{-|k_y(x-x')|}dx' \quad (81)$$

$$\simeq \frac{i}{2}\mu(\xi_{k_y}^+ - \xi_{k_y}^-)\text{sgn}(k_y), \text{ for } |x| \lesssim s \quad (82)$$

To derive the latter relation, the vorticity near the ‘‘step’’ at $x = s$ may be expanded as $\omega = \text{const} - \mu H(x - s - \xi^+) \simeq \mu\xi^+(y, t)\delta(x - s) + f(x)$ where $H(x)$ is Heaviside’s step function, $\delta(x) = dH/dx$ is Dirac’s delta function, and $f(x)$ denotes y -independent terms that may be discarded because $\text{sgn}(0) = 0$. The step at $x = -s$ contributes with the opposite sign. The exponential in equation (81) may be dropped because of inequality (78).

Even though ω varies rapidly with x , the u_x that it induces is independent of x . (More precisely, u_x decays exponentially in x on lengthscale $1/|k_y| \gg s$.) This result, which will simplify the analysis, corresponds to our earlier finding that swinging waves only contribute significantly when their phasefronts are radial. More generally, one observes from equation (81) that any vorticity distribution that is elongated in the streamwise direction induces a velocity field that is much smoother in the x -direction than is ω . The convolution smooths out variations in x with a smoothing length of $1/|k_y|$; hence u_x varies in x —as well as in y —on the scale $1/|k_y|$. One can further argue on dimensional grounds that, in general, elongated vorticity distributions produce a velocity field with amplitude $u_x \sim \omega\xi$. When $\xi = 0$, one must have $u_x = 0$ by symmetry considerations. And although there is a dimensionless combination $k_y s$ (where s would represent the lengthscale of ω in the x -direction), u_x cannot depend on s because it smooths out ω on scales much larger than s .

The simple equations (80) and (82) embody all the dynamics of the initial stages of the shear instability. To solve them, we insert the trial solution $\xi^\pm \propto e^{\gamma t}$, which produces for the eigenvector and eigenvalue

$$\xi_{k_y}^\pm \propto \frac{1}{\gamma \mp iqs k_y} \quad (83)$$

$$\gamma^2 = -(qs k_y)^2 - qs|k_y|\mu \quad (84)$$

The behavior of the growth rate γ is very similar to that found for previously considered vorticity profiles (eqs. [45], [73] and Fig. 8). When $\mu > 0$, i.e. when the perturbed vorticity and the background vorticity $-q$ have opposite

signs, the flow is stable for all k_y . When $\mu < 0$, the flow is unstable provided that

$$|k_y| < \kappa \equiv \frac{|\mu|}{qs}. \quad (85)$$

The maximum growth rate is $\gamma_{\text{max}} = |\mu|/2$, which occurs at $|k_y| = \kappa/2$, and γ falls to zero as either $k_y \rightarrow 0$ or $k_y \rightarrow \kappa$.

We may now begin to appreciate how the shear instability works in real space. Depending on the phases of the sine waves $\xi^+(y)$ and $\xi^-(y)$, the velocity field u_x that they induce can tend to amplify them. Figure 11 shows a growing mode in an unstable shear flow that has $\mu < 0$, so that the vorticity in the strip down the middle has the same sign as the background vorticity $-q$. The strip bulges in its central region, where $|y| \lesssim L_y/4$, and because of the sign of ω , the bulge tends to produce a swirling velocity around itself with the same sense as the background shear. Therefore it produces a positive u_x in the top of the figure, and a negative one at the bottom, as depicted in the right panel. Furthermore, the strip is tilted into the top-right and bottom-left quadrants of the $x - y$ plane. Although the tilt might not be obvious at first glance, if one compares the vorticity along any line of fixed $|y|$ with that at $-|y|$, one observes that the former is to the right of the latter. Because the induced u_x pulls the top half of the strip further to the right and the bottom half further to the left, it tends to amplify the tilt. In sum, u_x converts a bulge into a tilt. When $\mu < 0$, the tilt is into the shear, having the same sense as a leading wave.

To complete the picture, consider the effect of the background shear, which carries ξ^+ downwards at speed qs , and ξ^- upwards at the same speed. As long as the vorticity strip is tilted into the shear, the background shear converts a tilt into a bulge, thus completing the loop and allowing for exponential growth.

Based on the above picture, we may estimate the fastest growth time as $\gamma_{\text{max}}^{-1} \sim \xi^+/u_x \sim 1/|\mu|$ (eq. [82]). Advection of the two contours by the background shear can dephase them before growth can occur. Since the dephasing time is $t_{\text{dephase}} \sim 1/|qsk_y|$, it will be shorter than the fastest growth time if $|k_y|$ is sufficiently large. In other words, if $|k_y| \gtrsim |\mu|/qs$, the flow is stable, as found above.

6.2. Momentum and Energy for the Top-Hat

It is instructive to see how momentum and energy interact to trigger the shear instability. Not only does this give a deeper understanding of why the instability operates, it also gives a sense of the nonlinear outcome of the instability, since it quantifies the driving force behind it. Furthermore, the interaction between momentum and energy is generally important in accretion disks. Understanding how this works in a nontrivial incompressible flow might be helpful when considering more complicated effects, such as three dimensional motions, baroclinicity, or magnetohydrodynamics.

We first derive expressions for the momentum and energy in terms of the dynamical variables ξ^\pm , and show that the equations of motion (80) and (82) exactly conserve these quantities. Perturbations to the top-hat profile have y -momentum (per unit L_y and setting $\rho = 1$)

$$M \equiv \int (u_y - u_y|_{\xi^\pm=0})dx dy/L_y \quad (86)$$

$$= \int (\bar{u}_y - \bar{u}_y|_{\xi^{\pm}=0}) dx, \quad (87)$$

where the bar denotes a y -average,

$$\bar{\mathbf{u}}(x) \equiv \int_0^{L_y} \mathbf{u}(x, y) dy / L_y. \quad (88)$$

Since $\bar{u}_x = 0$ (because $u_x = -\partial_y \nabla^{-2} \omega$), the total x -momentum always vanishes, and need not be considered further. Henceforth we call M the momentum. From $\bar{\omega} = \partial_x \bar{u}_y$, we may express

$$\begin{aligned} \bar{u}_y - \bar{u}_y|_{\xi^{\pm}=0} &= \int_{-\infty}^x (\bar{\omega}(x') - \bar{\omega}(x'))|_{\xi^{\pm}=0} dx' \quad (89) \\ &= \mu \left(|\xi_{k_y}^-|^2 \delta(x+s) - |\xi_{k_y}^+|^2 \delta(x-s) \right) \quad (90) \end{aligned}$$

where the latter relation applies for a single k_y component of ξ^{\pm} (including the $-k_y$ piece). To derive it, note that the integrand in equation (89) vanishes everywhere except where a line of constant x' pierces either of the two contours. Considering first the vicinity of the ξ^+ contour, we have $\bar{\omega}(x') - \bar{\omega}(x')|_{\xi^{\pm}=0} = -\mu |\xi_{k_y}^+|^2 d\delta/dx|_{x'-s}$, after writing ω in terms of Heaviside's function as below equation (82), and then expanding. The contour ξ^- contributes the analogous amount, but with the opposite sign because the jump in vorticity across it is in the opposite sense. Therefore both steps contribute

$$M = M_- + M_+ \quad (91)$$

$$M_{\pm} \equiv \mp \mu |\xi_{k_y}^{\pm}|^2. \quad (92)$$

The overall signs of M_- and M_+ will play an important role in what follows. They are determined solely by the sign of the jump in vorticity across the corresponding step, independent of the functions ξ^- and ξ^+ . We may understand this as follows. To be definite, we consider first the step at $x = -s$ and set $\mu > 0$. Because $\bar{\omega} = d\bar{u}_y/dx$, the unperturbed \bar{u}_y is constant for $x < -s$ and has positive slope ($= \mu$) for $x > -s$. Any perturbation ξ^- must widen the range in x over which $\bar{\omega}$ makes a transition from 0 to μ . Hence it will widen the range over which \bar{u}_y increases in slope. Therefore the perturbed \bar{u}_y must exceed its unperturbed value and $M_- > 0$. Generalizing this reasoning, it is clear that wherever the unperturbed profile has a positive jump in vorticity, perturbations always contribute positive momentum; similarly, perturbed negative jumps contribute negative momentum.

The perturbed kinetic energy is

$$E \equiv \frac{1}{2} \int (-qx\hat{\mathbf{y}} + \mathbf{u})^2 - (-qx\hat{\mathbf{y}} + \mathbf{u})^2|_{\xi^{\pm}=0} dx dy \quad (93)$$

$$= E_- + E_+ + E_{u^2} \quad (94)$$

where

$$E_- + E_+ \equiv \int -qx(\bar{u}_y - \bar{u}_y|_{\xi^{\pm}=0}) dx \quad (95)$$

$$= qs\mu \left(|\xi_{k_y}^-|^2 + |\xi_{k_y}^+|^2 \right), \quad (96)$$

which follows from equation (90), and

$$E_{u^2} \equiv \int \frac{1}{2} (\bar{u}^2 - \bar{u}^2|_{\xi^{\pm}=0}) dx \quad (97)$$

$$= \frac{\mu^2}{2|k_y|} \left| \xi_{k_y}^- - \xi_{k_y}^+ \right|^2, \quad (98)$$

which follows from $u_{y,k_y} = (i/k_y) du_{x,k_y}/dx$ and equation (82) (including now the exponential previously dropped from equation (81)). There are two different kinds of energy. The first, composed of E_- and E_+ , is localized near each step in ω , and is due to changes in \bar{u}_y that are second order in ξ^{\pm} ; we call it the mean-flow energy. The second, $E_{u^2} \geq 0$, is spread out in x over a range $\sim 1/|k_y| \gg s$, and is due to the terms in \mathbf{u} that are first order in ξ^{\pm} ; we call it the perturbation energy.

The equations for ξ^{\pm} conserve momentum,

$$\frac{dM_{\pm}}{dt} = \pm F \quad (99)$$

where

$$F \equiv \text{sgn}(k_y) \frac{i}{2} \mu^2 \left(\xi_{k_y}^{+*} \xi_{k_y}^- - \xi_{k_y}^+ \xi_{k_y}^{-*} \right), \quad (100)$$

is the rate at which momentum flows from the step at $x = -s$ to the one at $+s$. In terms of more familiar variables, it can be shown that the x -dependent momentum flux $\overline{u_x u_y}$ is

$$\overline{u_x u_y} = \begin{cases} F & , \quad |x| < s \\ 0 & , \quad |x| > s \end{cases}, \quad (101)$$

which is in accord with equation (99). Similarly, the equations for ξ^{\pm} conserve energy,

$$\frac{d}{dt} (E_- + E_+) = -q(2s)F \quad (102)$$

$$= -\frac{dE_{u^2}}{dt}, \quad (103)$$

which may be understood as follows. Consider two streamlines of the unperturbed flow, one at $x = x_1$ and the other at $x = x_2$, with $x_1 < x_2$, and label their unperturbed y -velocities v_1 and v_2 . Their unperturbed specific energies (energy per unit mass) are then $v_1^2/2$ and $v_2^2/2$. We perturb the streamlines by transferring y -momentum from one streamline to the other. If the specific momentum transferred from x_1 to x_2 is Δv , then the change in mean-flow energy is

$$\begin{aligned} &\frac{(v_1 - \Delta v)^2 - v_1^2}{2} + \frac{(v_2 + \Delta v)^2 - v_2^2}{2} \\ &\approx (v_2 - v_1)\Delta v = -q(x_2 - x_1)\Delta v, \end{aligned} \quad (104)$$

which is equivalent to equation (102). When the momentum transfer tends to lower the relative velocity of the two streamlines (i.e., $\Delta v > 0$), energy is extracted from the mean flow. Conversely, when the transfer tends to increase the relative velocity, energy must be added to the mean flow.⁸ Of course, the total energy is conserved: if energy is extracted from the mean flow it must correspondingly increase E_{u^2} .

Let us see what the above results imply for the shear instability, first setting $\mu < 0$ so that the instability can operate. Perturbations to the step at $x = -s$ have negative momentum, and those at $x = s$ have positive momentum (eq. [92]). Therefore perturbations transfer momentum from $x = -s$ to $x = s$. Since this transfer tends to lower the relative velocity of the streamlines at $x = \pm s$, energy is extracted from the mean flow and added to E_{u^2} . This is the recipe for instability. However, for instability to actually occur the increase in E_{u^2} must balance the

⁸ Note that outward transport of angular momentum in an accretion disk is equivalent to a momentum transfer in a shear flow that tends to lower the relative velocity of two streamlines.

decrease in mean-flow energy. Since $E_{u^2} \propto 1/|k_y|$, this is only possible for sufficiently small $|k_y|$. Quantitatively, unstable perturbations must have $M_- + M_+ = 0$; otherwise, $M_- + M_+$ could not remain constant as $|\xi_{k_y}^\pm|$ grows. Therefore, $|\xi_{k_y}^-| = |\xi_{k_y}^+|$. Similarly, energy conservation implies $E_{u^2} + E_- + E_+ = 0$, or

$$|k_y| = \frac{-\mu}{2qs}(1 - \cos \phi), \quad (105)$$

where ϕ is the phase difference between $\xi_{k_y}^+$ and $\xi_{k_y}^-$; this relation also follows from equations (83)-(84). The largest $|k_y|$ occurs when $\phi = \pi$, and is equal to $\kappa = |\mu|/qs$, as for equation (85).

If $\mu > 0$, equation (105) can never be satisfied, and there is always stability, as implied by Fjørtoft's theorem (Drazin & Reid 2004). This seemingly mysterious behavior can also be understood from momentum and energy considerations. When $\mu > 0$, the perturbed momentum at $x = -s$ is positive, and that at $x = s$ is negative. Therefore any perturbation must transfer momentum from $x = s$ to $x = -s$, which enhances the background shear, and must increase the mean flow energy $E_- + E_+$. By energy conservation this is only possible if the perturbation energy E_{u^2} decreases, and since E_{u^2} is always positive, no perturbation can grow.

6.3. Numerical Simulation of the Top-Hat

Figure 12 shows the nonlinear evolution when the unperturbed vorticity is given by equation (75). The initial perturbation to the curves at $x = \pm s$ is unstable ($k_y = 0.75\kappa$), and wraps up into a vortex.

To make this figure we wrote a Lagrangian code, which can handle the rapid variations in ω more easily than can the pseudospectral code. The Lagrangian form of the equation of motion (eq. [8]) is $\partial_t \mathbf{x} = -qx\hat{\mathbf{y}} + \mathbf{u}$, where $\mathbf{x} = \mathbf{x}(\mathbf{x}_0, t)$ is now a function of the initial coordinate and time, ∂_t is taken at fixed \mathbf{x}_0 , and \mathbf{u} is determined by equation (9). We chose 2000 initial points along each of the two curves at $x = \pm s$, and evolved these points assuming periodic boundary conditions in y and open boundary conditions in x . Given \mathbf{x} for each of these points, we immediately know ω , since ω is locally conserved. To convert ω to \mathbf{u} , we evaluated equation (9) by interpolating ω onto a grid, taking the Fourier transform of ω , multiplying by the appropriate factors of \mathbf{k} , taking the inverse Fourier transform to yield \mathbf{u} on the grid, and finally interpolating from the grid back onto the curves. To check the code, we plot in Figure 12 at time= 3000 the eigenfunction

$$\xi^\pm(y) \propto \pm \cos \left(|k_y|y \mp \tan^{-1} \frac{\gamma}{qs|k_y|} \right) \quad (106)$$

(eq. [83]). These curves are indistinguishable from the code's output, implying agreement between code and theory. We have also checked that the growth rate at early times, while $\xi^\pm \lesssim s$, is $\xi^\pm \propto \exp(\gamma t)$, where $\gamma = 1/1200$ (eq. [84]). As usual, for our numerical results we measure time in units of Ω_0^{-1} , i.e., we set $q = 3/2$.

At late times, ω exhibits rapid spatial variations, and the boundaries that separate the regions where $\omega = 0$ from the ones where $\omega = \mu$ become more and more convoluted. The Lagrangian code has no viscosity; the evolution shown in Figure 12 breaks down at time $\gtrsim 10,000$ when

the curves are so convoluted that adjacent points on a curve are widely separated. If we were to include an explicit viscosity, it would wipe out the rapid variations in ω at late times, leaving a smooth vortex. At what stage the viscosity acts depends on how small the viscosity is. In astrophysical disks, the viscosity is extremely small, so if a shear instability acts, it might lead to extremely rapid variations in ω . Whether this is unstable to three dimensional perturbations is an interesting possibility.

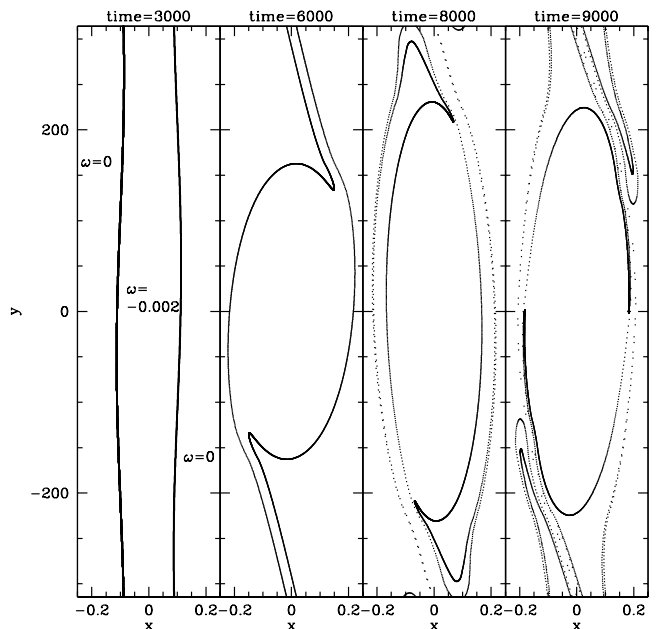


FIG. 12.— **Numerical Simulation of the Top-Hat:** The unperturbed vorticity is given by equation (75), with $s = 0.1$ and $\mu = -0.002$; the initial perturbation to the curves at $x = \pm s$, $\xi^\pm(y)$, are sinusoidal with $k_y = 0.01 = 0.75\kappa$, and amplitudes = 0.001. The initial perturbation is unstable to the shear instability, and wraps up into a vortex. The numerical simulation was done with a Lagrangian code described in the main text.

6.4. Infinite Number of Steps

Consider now the general case, in which the unperturbed ω is given by $\omega_{\text{unp}} = \omega^i$, for $x_i < x < x_{i+1}$, where ω^i and x_i are sets of constants with $i = 1, \dots, \infty$. As before, there is a curve $\xi^i(y, t)$ at each step x_i , whose equation of motion is, generalizing equation (80),

$$\left(\frac{d}{dt} - qx_i i k_y \right) \xi_{k_y}^i = u_{x, k_y}. \quad (107)$$

Equation (82) generalizes to

$$u_{x, k_y} = -\frac{i}{2} \text{sgn}(k_y) \sum_i \omega_\delta^i \xi_{k_y}^i. \quad (108)$$

where the jump in vorticity at step i is

$$\omega_\delta^i \equiv \omega^i - \omega^{i-1} \quad (109)$$

We continue to assume that $|k_y|s \ll 1$, where s is now the extent of the region of non-zero vorticity. To find instability, we set $\xi_{k_y}^i \propto e^{\gamma t}$, yielding for the eigenfunction and eigenvalue

$$\xi_{k_y}^i \propto \frac{1}{\gamma - qx_i i k_y} \quad (110)$$

$$1 = -\frac{i}{2} \text{sgn}(k_y) \sum_i \frac{\omega_\delta^i}{\gamma - qx_i i k_y}. \quad (111)$$

thus recovering the results derived with swinging waves (eqs. [67],[64]) when we make the identification $\gamma = \alpha q \bar{K}_y$.

6.5. Top-Hat With Wings

Because the top-hat vorticity profile has $\int \omega dx dy \neq 0$, it produces a velocity field u_y that is infinite in extent. Although this is somewhat disconcerting, profiles that do not suffer from this problem behave similarly to the top-hat. To illustrate, we consider the top-hat with wings, i.e.,

$$\omega_{\text{unp}} = \begin{cases} \mu & , \quad |x| < s \\ -\mu & , \quad s < |x| < 2s \\ 0 & , \quad 2s < |x| \end{cases} \quad (112)$$

which clearly integrates to zero. Figure 13 shows a numerical simulation of this profile, done with the Lagrangian code described in §6.3. See caption for details. For unstable initial conditions, the vorticity again tends to wrap up into a vortex.

It is perhaps not surprising that the infinite extent of the unperturbed u_y is not important, since the unperturbed u_y was not important for any of our three explanations of the shear instability, in §§5, 6.1, and 6.2.

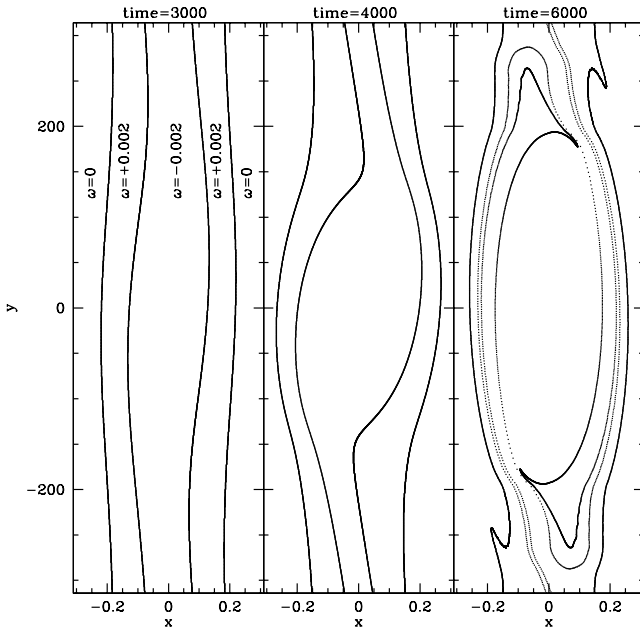


FIG. 13.— Numerical Simulation of Top-Hat with Wings: The unperturbed vorticity is given by equation (112), with $s = 0.1$ and $\mu = -0.002$; the initial perturbations are sinusoidal with $k_y = 0.01$. The dispersion relation (eq. [111]) shows that this situation is unstable, with growth rate $\gamma = 1/810$. We checked that at early times the numerical simulation reproduces this growth rate. As in Figure 12, the nonlinear outcome is a tightly wrapped vortex with convoluted boundaries.

7. CONCLUSION

Two dimensional shear flows are linearly stable, but nonlinearly unstable. Linear modes that are aligned with the shear (“axisymmetric”) have zero frequency; those that are not aligned (“swinging”) are transiently amplified before decaying. When the two couple nonlinearly, they are always unstable provided that the swinging mode’s azimuthal wavelength is long enough. If this is the case, the

swinging mode couples with the axisymmetric one to produce a new leading swinging mode with larger amplitude than itself, implying instability. Quantitatively, the criterion for instability is

$$\frac{k_{y,sw}}{k_{x,axi}} \lesssim \frac{|\omega|}{q} = \frac{|\omega|}{3\Omega/2} \quad (113)$$

where $|\omega|/q$ is the ratio of perturbed to background vorticity, and $k_{y,sw}/k_{x,axi}$ is the ratio of swinging-azimuthal to radial-axisymmetric wavenumbers. This shows that even when the amplitudes of the perturbations are vanishingly small, instability results for small enough $k_{y,sw}$.

When the instability is triggered, the swinging waves grow exponentially at the rate $\sim 1/|\omega|$, assuming that their wavelength is larger than the critical value (eq. [113]) by a factor of order unity. Eventually, regions of negative vorticity concentrate into vortices with increasingly convoluted boundaries. Since astrophysical disks have very little viscosity, such vortices might become turbulent in three dimensions before viscosity can act to smooth them.

In §6 we explained how the instability works in real space. When a nearly axisymmetric strip of perturbed vorticity has a small bulge, this bulge tends to tilt the strip. Advection of the tilted strip by the background shear reinforces the bulge when equation (113) holds, where $k_{x,axi}^{-1}$ is now interpreted as the width of the strip, and $k_{y,sw}$ is the azimuthal wavenumber of a perturbation to the strip. (It is also required that $\omega < 0$ if the strip only has a single sign of vorticity.) We also showed that the instability can be understood from momentum and energy considerations: when equation (113) holds and the strip is unstable, the momentum transferred from a streamline on one side of the strip to the other tends to lower the relative velocity of two streamlines (which is equivalent to transferring angular momentum outwards in an accretion disk), and therefore converts shear energy into perturbation energy.

It is tempting to speculate that this nonlinear instability might provide a route to turbulence. Perhaps vortices are unstable to three dimensional perturbations, and these perturbations can create new axisymmetric modes that are in turn unstable to the production of vortices. It is also possible that other effects are required. Perhaps vorticity is produced by convection or by stirring from planets, and if enough vorticity is produced, the disk becomes unstable in the manner described in this paper. Even if other effects are required, we feel that the technique introduced in this paper—the examination of couplings between swinging modes—will be helpful. It gives a well-defined procedure for analyzing nonlinear effects, both theoretically and numerically. Similar techniques might also be employed to give insight into other issues in shear flows, such as the nonlinear development of the magnetorotational instability.

We thank Gordon Ogilvie for showing us how easy it is to implement shearing box boundary conditions in a pseudospectral code, and Jeremy Goodman for helpful discussions at an early stage of this project. We also thank the referee for helpful suggestions.

APPENDIX

DESCRIPTION OF THE PSEUDOSPECTRAL CODE

The pseudospectral code simulates the 3-D shearing box equations of motion (eqs. [5]-[6]), though in the present paper we only present 2-D simulations. Most of our methods are standard, except for our new method for remapping modes that is both simpler and more accurate than that used by other investigators.

In our simulations, the unit of time is chosen so that

$$\Omega_0 = 1 , \quad (\text{A1})$$

and we also set the constant density

$$\rho = 1 . \quad (\text{A2})$$

Equations (5)-(6) are solved in a box of size $L_x \times L_y \times L_z$ that is subject to periodic boundary conditions in y and z ,

$$\mathbf{u}(x, 0, z) = \mathbf{u}(x, L_y, z) \quad (\text{A3})$$

$$\mathbf{u}(x, y, 0) = \mathbf{u}(x, y, L_z) \quad (\text{A4})$$

and to a shifted periodic (“shearing sheet”) boundary condition in x :

$$\mathbf{u}(0, y, z) = \mathbf{u}(L_x, (y - qtL_x) \bmod L_y, z) . \quad (\text{A5})$$

The modulus function “mod” is defined as follows:

$$(y - qtL_x) \bmod L_y \equiv y - qtL_x + pL_y \quad (\text{A6})$$

where p is the integer that makes the right-hand side of the above expression lie within the box in the y -dimension: $0 \leq y - qtL_x + pL_y < L_y$.

Changing to Lagrangian coordinates \mathbf{X}, T that shear with the background velocity $-qx\hat{\mathbf{y}}$ (eqs. [12]-[13]), equation (5) becomes

$$\frac{\partial \mathbf{u}}{\partial T} = 2u_y \hat{\mathbf{x}} - (2 - q)u_x \hat{\mathbf{y}} - \nabla_{\mathbf{x}} P - \mathbf{u} \cdot \nabla_{\mathbf{x}} \mathbf{u} , \quad (\text{A7})$$

where $\nabla_{\mathbf{x}} \equiv \nabla$ is a gradient with respect to \mathbf{x} , not \mathbf{X} .

Lagrangian coordinates (X, Y, Z) lie within a box of size $L_x \times L_y \times L_z$; the boundary conditions on the sides of this box are periodic in all three dimensions. The Fourier transform of \mathbf{u} with respect to \mathbf{X} is

$$\mathbf{u}_{J_x, J_y, J_z} \equiv \frac{1}{L_x L_y L_z} \int_{L_x \times L_y \times L_z} \mathbf{u} \exp(-i\mathbf{K} \cdot \mathbf{X}) d^3 \mathbf{X} , \quad (\text{A8})$$

where the wavevector \mathbf{K} takes on the discrete values

$$K_x = \frac{2\pi}{L_x} J_x , \quad K_y = \frac{2\pi}{L_y} J_y , \quad K_z = \frac{2\pi}{L_z} J_z , \quad (\text{A9})$$

with J_x, J_y, J_z integers. Hence the Fourier transform of equation (A7) with respect to \mathbf{X} is

$$\frac{d\tilde{\mathbf{u}}}{dT} = 2\tilde{u}_y \hat{\mathbf{x}} - (2 - q)\tilde{u}_x \hat{\mathbf{y}} - i\mathbf{k}(\mathbf{K}, T)\tilde{P} - i\mathbf{k}(\mathbf{K}, T) \cdot \widetilde{\mathbf{u}\mathbf{u}} , \quad (\text{A10})$$

where, for clarity, we denote Fourier transforms with a tilde instead of the subscripts J_x, J_y, J_z . The (x, y, z) components of the wavevector $\mathbf{k}(\mathbf{K}, T)$ are defined as follows

$$\mathbf{k}(\mathbf{K}, T) \equiv (K_x + qTK_y, K_y, K_z) . \quad (\text{A11})$$

The last term in equation (A10) has been written in a tensor form; it represents a vector whose j 'th component is

$$-i \sum_{l=1}^3 k_l \tilde{u}_l \widetilde{u}_j , \quad (\text{A12})$$

where $\widetilde{u_l u_j}$ is the Fourier transform of the product $u_l u_j$. Equation (A10) is supplemented by the Fourier-space version of equation (6):

$$\mathbf{k}(\mathbf{K}, T) \cdot \tilde{\mathbf{u}} = 0 \quad (\text{A13})$$

The numerical code evolves equation (A10) in time using second-order Runge-Kutta, with \tilde{P} determined by the incompressibility constraint (eq. [A13]). Equation (A10) is integrated for $n_x \times n_y \times n_z$ different modes, each of which is labelled by the integers (J_x, J_y, J_z) , with $-n_x/2 < J_x \leq n_x/2$, $-n_y/2 < J_y \leq n_y/2$, and $-n_z/2 < J_z \leq n_z/2$.⁹

The code equations differ from the exact equations (A8)-(A13) in two ways. First, the Fourier transform in the code is the discretized version of equation (A8):

$$\mathbf{u}_{J_x, J_y, J_z} \equiv \frac{1}{n_x n_y n_z} \sum \mathbf{u}(\mathbf{X}) \exp(-i\mathbf{K} \cdot \mathbf{X}) , \quad (\text{A14})$$

⁹ In truth, only half of these modes are simulated, which makes the code run twice as fast as it otherwise would. The other half that are not simulated are determined by the condition that the components of \mathbf{u} are real, not complex, numbers. But for the purposes of the discussion in the present section, we ignore this complication.

with the sum taken over $n_x \times n_y \times n_z$ discrete Lagrangian points \mathbf{X} . And second, k_x is not given $K_x + qTK_y$, as would be inferred from equation (A11). In this respect, our code differs from other codes (e.g., Rogallo 1981; Umurhan & Regev 2004; Barranco & Marcus 2006). A single mode with a given (J_x, J_y, J_z) has the following spatial dependence

$$\exp\left(2\pi i \left(\frac{J_x X}{L_x} + \frac{J_y Y}{L_y} + \frac{J_z Z}{L_z}\right)\right) \quad (\text{A15})$$

$$= \exp\left(2\pi i \left(\left(\frac{J_x}{L_x} + qT\frac{J_y}{L_y}\right)x + \frac{J_y}{L_y}y + \frac{J_z}{L_z}z\right)\right). \quad (\text{A16})$$

In substituting for Y with equation (12), the modulus term may be dropped because it does not contribute to the exponential. By the same token, we can replace J_x on the right-hand side of the above expression with $J_x + pn_x$, where p is any integer, without affecting the exponential. (Note that $x = \{0, 1, \dots, n_x - 1\}L_x/n_x$.) This is the well-known phenomenon of aliasing. So instead of equation (A11) for k_x , we can equally well use a similar expression, but with $J_x \rightarrow J_x + pn_x$. The value of p should be chosen so that the physical wavenumber k_x is shifted as close as possible to zero. Other p 's correspond to lengthscales smaller than the grid's scale. Hence,

$$k_x \equiv \frac{2\pi}{L_x} \left(\left(J_x + qT J_y \frac{L_x}{L_y} \right) \widehat{\text{mod}} n_x \right), \quad (\text{A17})$$

where $\widehat{\text{mod}}$ is a modulus operator:

$$J \widehat{\text{mod}} n_x \equiv J + pn_x, \quad (\text{A18})$$

with p an integer such that $-n_x/2 < J + pn_x \leq n_x/2$. (These limits differ from those used to define the earlier modulus operator below eq. [A6].) Since other authors use $k_x = K_x + qTK_y$ instead of equation (A17) for k_x , the k_x of each of their modes grows to large positive or negative values. To stop this growth, they periodically remap the modes to small k_x . But this has the undesirable consequence that the distribution of k_x 's that is being used to simulate the fluid changes substantially from just after a remapping event to just before the subsequent remapping. Conversely, with equation (A17) there is no need for an explicit remapping; in effect, the remapping is done automatically by the modulus operator.

The nonlinear term in equation (A10), written explicitly in equation (A12), is evaluated using the standard pseudospectral method (e.g., Maron & Goldreich 2001, and references therein): after dealiasing (see below), $\mathbf{u}_{J_x, J_y, J_z}$ is transformed into \mathbf{u} by performing an inverse fast Fourier transform (FFT). Then, the product $u_i u_j$ is formed in real space, and finally the FFT of this product is taken.

To prevent aliasing errors when evaluating the nonlinear term, $\mathbf{u}_{J_x, J_y, J_z}$ is truncated just before the time derivative is evaluated by setting to zero any mode whose $|k_x|$, $|k_y|$, or $|k_z|$ exceeds $2/3$ of its maximum value—the standard “2/3-rule”; explicitly, $\mathbf{u}_{J_x, J_y, J_z} \rightarrow 0$ wherever one of the following hold

$$|J_y| > \frac{n_y}{3} \quad (\text{A19})$$

$$|J_z| > \frac{n_z}{3} \quad (\text{A20})$$

$$\left| \left(J_x + qT J_y \frac{L_x}{L_y} \right) \widehat{\text{mod}} n_x \right| > \frac{n_x}{3} \quad (\text{A21})$$

The last condition above follows from equation (A17). Note that the k_x of a mode is remapped by the modulus operator from $+k_x$ to $-k_x$ when $\left| \left(J_x + qT J_y \frac{L_x}{L_y} \right) \widehat{\text{mod}} n_x \right| = n_x/2$. Such modes have had their amplitude set to zero because they satisfy the inequality of equation (A21). Hence there is no danger that remapping artificially introduces power into leading modes.

REFERENCES

- Afshordi, N., Mukhopadhyay, B., & Narayan, R. 2005, *ApJ*, 629, 373
 Balbus, S. A. & Hawley, J. F. 1998, *Reviews of Modern Physics*, 70, 1
 Balbus, S. A. & Hawley, J. F. 2006, *ApJ*, 652, 1020
 Barranco, J. A. & Marcus, P. S. 2006, *Journal of Computational Physics*, 219, 21
 Chagelishvili, G. D., Zahn, J.-P., Tevzadze, A. G., & Lominadze, J. G. 2003, *A&A*, 402, 401
 Drazin, P. G. & Reid, W. H. 2004, *Hydrodynamic Stability* (*Hydrodynamic Stability*, by P. G. Drazin and W. H. Reid, pp. 626. ISBN 0521525411. Cambridge, UK: Cambridge University Press, September 2004.)
 Gammie, C. F. & Menou, K. 1998, *ApJ*, 492, L75+
 Gill, A. E. 1965, *Journal of Fluid Mechanics*, 21, 503
 Hawley, J. F., Balbus, S. A., & Winters, W. F. 1999, *ApJ*, 518, 394
 Ioannou, P. J. & Kakouris, A. 2001, *ApJ*, 550, 931
 Ji, H., Burin, M. J., Schartman, E., & Goodman, J. 2006, *Nature*, 444, 343
 Johnson, B. M. & Gammie, C. F. 2005, *ApJ*, 635, 149
 Lesur, G. & Longaretti, P. Y. 2005, *A&A*, 444, 25
 Maron, J. & Goldreich, P. 2001, *ApJ*, 554, 1175
 Mukhopadhyay, B., *ApJ*, 653, 503
 Pullin, D. I. 1992, *Annual Review of Fluid Mechanics*, 24, 89
 Rogallo, R. S. 1981, *NASA STI/Recon Technical Report N*, 81, 31508
 Sano, T., Miyama, S. M., Umabayashi, T., & Nakano, T. 2000, *ApJ*, 543, 486
 Shen, Y., Stone, J. M., & Gardiner, T. A. 2006, *ApJ*, 653, 513
 Umurhan, O. M. & Regev, O. 2004, *A&A*, 427, 855
 Yecko, P. A. 2004, *A&A*, 425, 385